Viscosity and Diffusion: Crowding and Salt Effects in Protein Solutions

Marco Heinen,[a] Fabio Zanini,[b] Felix Roosen-Runge,[b] Diana Fedunová,[c] Fajun Zhang,[b] Marcus Hennig,[b,d] Tilo Seydel,[d] Ralf Schweins,[d] Michael Sztucki,[e] Marián Antalík,[c,f] Frank Schreiber,[†b] and Gerhard Nägele[*a]

Received Xth XXXXXXXXXX 20XX, Accepted Xth XXXXXXXXX 20XX
First published on the web Xth XXXXXXXXXX 200X
DOI: 10.1039/b000000x

We report on a joint experimental-theoretical study of collective diffusion in, and static shear viscosity of solutions of bovine serum albumin (BSA) proteins, focusing on the dependence on protein and salt concentration. Data obtained from dynamic light scattering and rheometric measurements are compared to theoretical calculations based on an analytically treatable spheroid model of BSA with isotropic screened Coulomb plus hard-sphere interactions. The only input to the dynamics calculations is the static structure factor obtained from a consistent theoretical fit to a concentration series of small-angle X-ray scattering (SAXS) data. This fit is based on an integral equation scheme that combines high accuracy with low computational cost. All experimentally probed dynamic and static properties are reproduced theoretically with an at least semi-quantitative accuracy. For lower protein concentration and low salinity, both theory and experiment show a maximum in the reduced viscosity, caused by the electrostatic repulsion of proteins. On employing our theoretical and experimental results, the applicability range of a generalized Stokes-Einstein (GSE) relation connecting viscosity, collective diffusion coefficient, and osmotic compressibility, proposed by Kholodenko and Douglas [Phys. Rev. E, 1995, **51**, 1081] is examined. Significant violation of the GSE relation is found, both in experimental data and in theoretical models, in concentrated systems at physiological salinity, and under low-salt conditions for arbitrary protein concentrations.

1 Introduction

A quantitative understanding of the dynamics in concentrated solutions of interacting proteins is of importance to the evaluation of cellular functions, and the improvement of drug delivery. Transport properties such as collective and self-diffusion coefficients, and the static and high-frequency shear viscosities, are strongly affected by the aqueous environment[1], and in particular by crowding effects due to high concentration of macromolecules, coupled both by direct and solvent-mediated, hydrodynamic interactions (HIs)[2–4]. The latter type of interaction, which is both long-ranged and of many-body nature, poses a particularly challenging task to a theoretical treatment of diffusion and rheological transport properties.

In the present paper, we report on a combined experimental and theoretical study on collective diffusion, low shear-rate static viscosity, and static and dynamic scattering functions of concentrated solutions of bovine serum albumin (BSA) proteins. The goal of this study is twofold. On the one hand, we explore how far a simple colloidal model in combination with state-of-the-art theoretical schemes can capture the microstructure and dynamics of proteins in solution. On the other hand, we investigate the concentration- and salt-dependence of collective diffusion and the static shear viscosity, and use our results to assess the applicability range of a generalized Stokes-Einstein (GSE) relation which combines the collective diffusion coefficient with the isothermal osmotic compressibility and the shear viscosity.

BSA is a protein which is readily soluble in water and stable over a wider range of protein concentrations at lower salt content. At higher salt content, however, it has the tendency to form dimers and oligomers. Its stability and reproducibility make it well-suited as a model system of globular proteins.

Proteins constitute identical solute units surpassing any synthetic colloid suspension in terms of monodispersity. In this respect, they are ideally suited to the application of analytical theoretical models used with good success for large colloids.

[a] *Institute of Complex Systems (ICS-3), Forschungszentrum Jülich, D-52425 Jülich, Germany*
[b] *Institut für Angewandte Physik, Universität Tübingen, 72076 Tübingen, Germany*
[c] *Institute of Experimental Physics, Slovak Academy of Sciences, 04353 Košice, Slovakia*
[d] *Institut Laue-Langevin, 38042 Grenoble Cedex 9, France*
[e] *European Synchrotron Radiation Facility, 38043 Grenoble Cedex 9, France*
[f] *Department of Biochemistry, Faculty of Sciences, P. J. Šafárik University, Moyzesova 11, 04154 Košice, Slovakia*
[†] frank.schreiber@uni-tuebingen.de
[*] g.naegele@fz-juelich.de

However, the construction of a quantitatively accurate theoretical model for protein solutions is considerably obstructed not only by the potential presence of impurities and oligomers, but also by the complex internal conformation and surface of a protein. The folding state depends on various control parameters such as temperature, protein concentration, pH value, and salinity. The irregular protein surface implies an orientation-dependent protein interaction energy with repulsive and attractive parts, and furthermore complicates the description of hydrodynamically influenced transport properties.

In a first step towards calculating dynamic properties of proteins, it is nonetheless possible to use a model of reduced complexity, with system parameters such as the pH-dependent particle charge determined from a consistent fit of theoretical expressions for the scattered intensity to the experimental static scattering functions. We use here a simple colloid model where the BSA interactions are described by the repulsive, electrostatic plus hard-core part of the isotropic Derjaguin-Landau-Verwey-Overbeek (DLVO) potential[5]. The effect of the non-spherical shape of BSA proteins is accounted for in the static intensity calculations within the so-called translational-orientational decoupling approximation, by describing the proteins as oblate spheroids interacting by a spherically symmetric effective pair potential.

Using this simplifying protein interaction model, the static structure factor, $S(q)$, entering into the static scattered intensity, is calculated as a function of wavenumber q, by using our newly developed modified penetrating background corrected rescaled mean spherical approximation (MPB-RMSA). This analytical method has been shown to be in excellent accord with numerically expensive computer simulation results for $S(q)$[6,7]. The system parameters of the protein-interaction model, most notably the effective protein charge, are determined from adjusting the theoretically calculated static intensity, $I(q)$, to the experimental one. The consistent agreement of calculated values and small-angle X-ray scattering (SAXS) data for $I(q)$ in a wide range of concentrations and wavenumbers indicates that left-out attractive interaction contributions are of minor importance at the considered salinities. As an independent additional check, the static light scattering (SLS) data for $S(q)$ at low q are found to be well reproduced by the theoretical fits of the SAXS data.

Without any further adjustment, the analytically calculated static structure factors are used as the only input to our theoretical calculations of the collective diffusion coefficient, d_C, and the low shear-rate limiting static viscosity η. To calculate d_C and the high-frequency part, η_∞, of the static viscosity, we use two approximate analytical schemes, namely the pairwise additive hydrodynamic interaction (PA) approximation, and the so-called self-part corrected $\delta\gamma$ method. As shown by two of the present authors[8], these two methods give results which are in general in good agreement with more elaborate Stokesian Dynamics simulation results for particles with Yukawa-type pair interactions.

The static viscosity,

$$\eta = \eta_\infty + \Delta\eta, \tag{1}$$

consists of a short-time part, η_∞, determined solely by hydrodynamic interactions (HIs), and a shear-stress relaxation part $\Delta\eta$, with $\Delta\eta > 0$. We calculate the latter using mode-coupling theory (MCT), which, like the two employed short-time schemes, requires $S(q)$ as the only input.

Our comparison with the experimental d_C measured by dynamic light scattering (DLS), and with η obtained from viscometry, is a stringent test for our theoretical results and for the employed isotropic interaction model, since except for the static input, no fit parameters are involved. In particular, no further adjustments of the theoretical predictions have been made on referring to the actually non-spherical shape of BSA proteins. We show that despite the simplicity of our model, most dynamic features are well reproduced by the theoretical results, to an at least semi-quantitative accuracy. In particular, both a low-concentration maximum of the reduced viscosity, and a maximum in d_C at a different concentration, are well captured by the theory.

We note here that in the past, several experimental studies of collective diffusion in BSA solutions[9–12,12,13] have been analyzed on basis of more approximate analytic expressions for the hydrodynamic interactions, for charged particles in form of far-field expansions of the translational two-body mobility tensors truncated after a few terms. In more recent studies, Bowen and Mongruel[14], and Yu et al.[15], have calculated the collective diffusion coefficient in conjunction with a detailed discussion of various direct interaction contributions to the osmotic compressibility factor, $S(q \to 0)$, entering into d_C. Their treatment of the salient hydrodynamic, i.e., sedimentation coefficient contribution, to d_C is still quite approximate, since it relies on a spherical cell model expression for ordered neutral spheres[16], and on an empirical expression for the sedimentation coefficient of charged spheres. The experimental results in the present paper are consistent with the earlier findings, but are unparalleled regarding the statistics, and the range of explored protein volume fractions and added salt concentrations. Only the good quality of our scattering data in combination with our elaborate viscosity data has allowed for a reliable comparison to our state-of-the-art theoretical results. The theoretical approach used in this work goes significantly beyond earlier theoretical work on BSA protein diffusion and viscosity, foremost regarding the thorough hydrodynamic treatment, but also regarding the high quality of the static structure factor input.

For BSA, also the short-time self-diffusion has been found to be reasonably well described by a simple spheroid model[17,18]. Of course, this does not imply that the complex

conformation of a globular protein plays no role. The DLVO model, even with inclusion of van der Waals attraction, is not sufficient to fully explain the rich phase behavior of proteins [19,20]. For example, it has been shown that surface patchiness has an important effect on the phase diagram [20]. Also, binding of multivalent ions to the protein surface can give rise to non mean-field behaviors beyond DLVO, such as charge inversion, re-entrant condensation and liquid-liquid phase separation [21–23].

Generalized Stokes-Einstein (GSE) relations, which approximately relate diffusion to rheological properties in concentrated complex liquids, are an important issue in microrheological studies, since a valid GSE relation allows to infer a rheological property more easily from diffusion measurements. Several GSE relations in colloidal dispersions of electrically neutral (porous and non-porous) spheres, and charged particle suspensions have been explored [24–27]. We study here a GSE relation not discussed in this earlier work, which has been proposed by Kholodenko and Douglas [28]. This GSE relation, which we refer to in the following as the KD-GSE relation, has been used in the biophysical and soft matter community [29–32]. It relates d_C to η, and to the square-root of the isothermal osmotic compressibility.

We present a thorough discussion of the applicability range of the KD-GSE relation for BSA solutions, and for generic colloidal fluids of solvent-impermeable spherical particles with screened Coulomb interactions, for a large range of salinities. Both the short-time and the long-time versions of the KD-GSE relation are considered. At high salinity, where the electrostatic interaction of particles is strongly screened, we find these two relations to become invalid at larger concentrations. At lower salinity, the KD-GSE relations are poorly satisfied even at low concentrations.

The paper is organized as follows. Sec. 2 includes the experimental details of the sample preparation, and of the SLS, DLS, SAXS, and rheological measurements. In Sec. 3, we discuss the employed simplifying model of BSA, and present the essentials of our theoretical methods, allowing for a fast calculation of measured static and dynamic properties. Our experiment data are shown in combination with the theoretical results in Sections 4 and 5, dealing with static and dynamic properties, respectively. Sec. 5 includes the examination of the KD-GSE relation. Our conclusions are contained in Sec. 6.

2 Experimental details

Sample preparation

BSA is a globular protein with a linear extension of about 7 nm. The considered aqueous solutions of BSA with no added salt, and with monovalent added salt such as NaCl, have a pH in between 5.5 and 7. Under these conditions, BSA is stable in solution, folded in its native state, and carrying a negative net charge in the range of roughly 8 to 20 elementary charge units (see below for details) [33,34]. BSA was purchased from Sigma (cat. A3059) as a lyophilized powder, certified globulin- and protease free.

The sample preparation for all experimental techniques started with the dissolution of protein powder in a solvent, and subsequent waiting until the solution was homogenized. The protein mass concentration, c_p, in the solution volume, $V_{\mathrm{H_2O}} + m_p \cdot \theta$, is given by the BSA mass m_p via

$$c_p = \frac{m_p}{V_{\mathrm{H_2O}} + m_p \cdot \theta} \quad , \tag{2}$$

where the specific protein volume $\theta = 0.74$ ml/g [35] determines the self-volume of proteins upon dissolution.

For small-angle X-ray scattering, deionized and de-gased water was used as solvent. The samples with concentrations higher than 15 mg/ml were prepared directly, while smaller concentrations were prepared from a stock solution of 18 mg/ml. The samples were filled into a plastic syringe and inserted into the capillary during the measurement.

For the viscosity measurements, the solutions were prepared similarly using as solvent both deionized water, and solutions of NaCl in deionized water. The NaCl molarity is calculated from the total solution volume, including the protein self-volume. All solutions used for the viscosity experiments were further de-gased by a water-jet air-pump.

For our light scattering experiments, stock solutions of BSA proteins in deionized water were mixed with solutions of NaCl in deionized water according to the required concentration. The NaCl molarity is calculated from the total water volume. Then, every sample was pressed with a plastic syringe through a hydrophilized nylon membrane filter with a pore size of 100 nm (Whatman Puradisc 13), and transferred into a cylindrical glass scattering cell. The cell was sealed immediately with a plastic cap.

The effect of the difference in NaCl concentrations between light scattering and viscosity samples, arising from the slightly differing sample preparation, is negligibly small.

Protein solutions often contain considerable amount of dimers and oligomers. The fraction of dimers and other oligomers in commercial BSA products has been carefully analyzed, e.g., by Hunter and Carta [36], who find a mass fraction of 6.4% of oligomers for the BSA product from Sigma used in this work. A purification scheme involving gel filtration has been successfully applied by Neal et al. [10], and Placidi and Cannistraro [12], to obtain the monomer fraction as a monodisperse model system. However, the preparation method by Neal et al. would be quite time-consuming and very delicate under our experimental conditions (dialysis against deionized water), in particular since we apply many different techniques (namely, DLS, SAXS, neutron scattering and viscometry) to

the same samples. Therefore, and similar to the light scattering studies in Refs.[11,13], our sample preparation follows a more direct and simple way, i.e. dissolution of the protein powder and removal of big aggregates with a membrane filter. This preparation has allowed us to reach very low salt concentrations, which after gel filtration with the connected buffer conditions would have required an exhaustive dialysis, and could have caused further problems, in particular in the case of de-ionized water. Our protein solutions, although perhaps slightly more polydisperse, represent thus an experimentally well-defined and well characterized model system, with a large accessible range of salt concentrations. The polydispersity effects are included in our fit functions for the purpose of describing the polydisperse experimental protein solution with the monodisperse theoretical model system.

Static and dynamic light scattering

Multi-angle dynamic light scattering (DLS) was performed at various concentrations of protein and added salt, at a temperature of $T = 295$ K. In particular, the BSA mass concentration, c_p, was chosen between 0.1 to 150 mg/ml, and the concentration of added salt was 0 (no added salt), 5, 150 and 500 mM. Note that, even in the zero added-salt case, the analysis of the scattering data discussed in Sec. 4 reveals a residual electrolyte concentration of a few mM, scaling roughly linear with c_p (see Table 1). This suggests a few possible sources of the residual electrolyte ions. Firstly, a possible source could be the surface-released counterions of charged BSA oligomers, not contained in our monodisperse model. Secondly, a salt contamination of the BSA stock, and thirdly the dissociation of acidic or alkaline surface groups off the BSA proteins cannot be excluded.

Static light scattering (SLS) experiments were performed on the same samples. We used a combined SLS/DLS device from ALV (goniometer: CGS3, correlator: 7004/FAST), located at the Institut Laue Langevin in Grenoble, with a minimum correlation time of 3.125 ns as initial and shortest time. The HeNe laser was operating at wavelength $\lambda_0 = 632.8$ nm, with an output power of 22 mW. The accessible range for the scattering angle (wavenumber) was 30 - 150° (q = 0.007 - 0.026 nm^{-1}). Moreover, the DLS intensity autocorrelation function decays on a time scale much slower than the interaction time, $\tau_I \sim \sigma_{d_0}^2/(4d_0) \sim 0.3$ μs, of BSA, where d_0 is the single protein average translational free-diffusion coefficient, and σ_{d_0} is an effective hydrodynamic diameter. Hence, in the $q \to 0$ limit, DLS probes the long-time collective diffusion coefficient d_C^L of BSA.

The coefficient d_C^L, also referred to as the gradient diffusion coefficient, quantifies the long-time decay of long-wavelength, isothermal protein concentration fluctuations. While, in principle, d_C^L needs to be distinguished from its short-time counterpart d_C^S, with $d_C^L \leq d_C^S$, it has been shown[37,38] that the relative difference is very small ($\lesssim 5\%$) even in highly concentrated systems. For solutions like the ones considered in this work, where non-pairwise additive HI contributions are small, $d_C = d_C^L$ becomes practically identical to d_C^S. This allows us to use more simple short-time dynamic methods for calculating d_C.

The normalized intensity autocorrelation function obtained from DLS,

$$g_2(q,t) = \frac{\langle I(\mathbf{q},0)I(\mathbf{q},t)\rangle}{\langle I(\mathbf{q})\rangle^2},$$

was fitted according to the Siegert relation, by the double exponential decay function

$$g_2(q,t) - 1 = \left(\sum_{i=1,2} A_i \cdot \exp\left[-D_i q^2 t\right] \right)^2 + \mathrm{B}, \qquad (3)$$

with decay constants D_1 and D_2, and amplitudes A_1 and A_2. The fit results were essentially the same with and without the background-correction constant B. At all probed angles, the two decay constants are widely separated ($D_1 \gtrsim 10 \times D_2$). The faster mode, D_1, is attributed to the (long-time) collective diffusion coefficient, d_C, of BSA monomers. The appearance of the slower mode characterized by D_2, can be attributed to the slow motion of the larger impurities and oligomers. After having checked that D_1 is overall q-independent within the experimental resolution, it was averaged with respect to its residual scattering angle fluctuations to gain better statistics.

Small-angle X-ray scattering

Aqueous solutions of BSA with mass concentrations between 0.9 mg/ml and 270 mg/ml, and without added salt, were measured by small-angle X-ray scattering (SAXS), at the beam line ID02 of the European Synchrotron Radiation Facility (ESRF) in Grenoble, France. The standard configuration at a 2m sample-to-detector distance, and a photon energy of 16051 eV was used. Measurements were repeated several times in the flow mode and with short detection times to ensure the absence of radiation damage. The data from the CCD were processed with the standard routines available at the beam line for radially averaging the data and correcting for transmission. Repeated measurements were summed up, and the solvent scattering was measured independently and subtracted from the data. Additionally, two dilute samples (at $c_p = 1$ and 2 mg/ml) with 150 mM of added NaCl were measured for form factor fitting.

Viscosity measurements

The viscosity data were measured at $T = 25°$ C, for different concentrations of protein and added salt. The first data set was

obtained for solutions without added salt, while the second set describes systems with 150 mM NaCl. All measurements were performed at a shear rate of 60 Hz $\ll 1/\tau_I$, using the suspended Couette-type viscometer described in Ref.[39]. The important advantage of this instrument is the possibility to measure the viscosity with a nearly homogeneous shear rate. In contrast, capillary methods or methods with falling probes do not guarantee homogeneity of shear rates. For capillary viscometers, e.g., the shear rate is zero at the capillary axis and maximal at its surface. Our device, where the rotor is fully immersed in the sample solution, works under nearly constant shear rate, without exhibiting surface effects, which would otherwise occur especially at higher protein concentrations. A test made for $c_p \approx 20$ mg/ml and 100 mg/ml, without salt and for 2M added NaCl, revealed no shear-rate dependence of the viscosity for shear rates between 50 and 95 Hz. This is consistent with the recent study in[40], where the BSA solution viscosity has been found to be independent of the shear rate in the concentration interval of 1 - 400 mg/ml, for shear rates of 47 - 4700 Hz .

The precision of the viscosity measurements is approximately 0.1%. In order to minimize systematic errors, every measurement was repeated three times, including separate sample preparations. The viscometer directly measures the relative shear-viscosity of the solution against pure water (for technical details see Ref.[39]). For the aqueous BSA solutions without added salt discussed in this work, the relative viscosity was directly measured. For BSA solutions with added salt, this quantity was obtained as the ratio of the following two values: (a) the directly measured relative viscosity of the BSA solution with salt against water divided by (b) the directly measured relative viscosity of the salt solution (without BSA) against water. We have checked that our BSA viscosity data are in good overall agreement with corresponding viscosity data on similar human serum albumin (HSA) solutions described in[41]. In this HSA study, a glass capillary microviscometer has been used.

3 Theory

Single-particle properties

In the following, we discuss the spheroid model of BSA. We use this model for the form factor fitting, and in determining effective sphere diameters related to different single-particle properties.

At low protein concentration and sufficient amount of added salt, inter-protein correlations are negligible. The scattered intensity, $I(q)$, is then solely determined by the form factor P, i.e. $I(q) \propto P(q)$. Crystallographic measurements[42–44] have revealed a flat and roughly heart-shaped structure of albumins. The computation of single-particle properties with an account of the highly complex particle shape of biomolecules can be done by numerical simulations only and is beyond the scope of this paper[43,45]. Rather, the aim of the present study is to give an essentially analytic description of the microstructure and the dynamics of interacting BSA proteins with low computational cost. We therefore intentionally choose an extremely simple model for the fit of the protein form factor, by an oblate, solid ellipsoid (spheroid). Clearly, this mapping of the complex protein configuration onto a simple geometric shape is a delicate and broad topic on its own. Considering that the focus of the present work is on collective correlations rather than on single-particle properties, we cannot discuss all details of this subtle matter; we basically follow the approach of Ref.[46].

For a homogeneously scattering spheroid with dimensions a and b, where a denotes the semi-axis of revolution, the orientationally averaged form factor, P_{ell}, is given by[47]

$$P_{ell}(q) = \int_0^1 d\mu |f(q,\mu)|^2 \tag{4}$$

with the scattering amplitude $f(q,\mu) = 3j_1(u)/u$, and $u = q\sqrt{a^2\mu^2 + b^2(1-\mu^2)}$. Here, j_1 is the spherical Bessel function of the first kind.

The fit of Eq. (4) to our newly recorded, low-concentration SAXS intensities at $c_p = 1$ and 2 mg/ml, and for 150 mM of added NaCl, is shown in Figure 1 of Sec. 4, along with a discussion of the obtained best fit values $a = 1.75$ nm and $b = 4.74$ nm.

When protein correlations come into play at higher concentrations or lower salinities, the spheroid model of BSA becomes too complex for an analytic treatment. Therefore, as far as the protein-protein interactions are concerned, we describe the proteins as effective spheres with diameter σ. Depending on the considered single-particle property, different definitions for σ can be given.

Consider first the geometric effective diameter, $\sigma_{geo} = 8(ab^2)^{1/3} = 6.80$ nm, which follows from equating the volume of the effective sphere to that of the spheroid. This effective diameter reflects the volume of the protein and the hydration layer visible to SAXS, but does not include thermo- and hydrodynamic effects of non-sphericity[48,49]. Thus, it should be considered as a lower boundary to the effective sphere diameter.

A thermodynamic effective diameter, $\sigma_{B_2} = 7.40$ nm, follows from demanding equal second virial coefficients, $B_2(T)$, of hard spheroid and effective hard sphere[50].

Alternatively, dynamic single-particle properties can be used in defining the effective diameter. For hydrodynamic stick-boundary conditions and $a < b$, the translational free diffusion coefficient of an isolated spheroid reads[43,51,52]

$$d_0^{ell}(a,b) = \frac{k_B T S(a,b)}{12\pi\eta_0 a}, \tag{5}$$

with absolute temperature T, Boltzmann's constant k_B, solvent shear-viscosity η_0, $S(a,b) = 2$ atan $\xi(a,b)/\xi(a,b)$ and $\xi(a,b) = \sqrt{|a^2-b^2|}\ /a$. Equating d_0^{ell} to the diffusion coefficient, $d_0 = k_BT/(3\pi\eta_0\sigma_{d_0})$, of an effective sphere gives $\sigma_{d_0} = 7.38$ nm.

Finally, one can derive another effective diameter from the intrinsic viscosity

$$[\eta] = \lim_{\phi\to 0}\frac{\eta(\phi)-\eta_0}{\eta_0\phi}, \tag{6}$$

where ϕ is the particle volume fraction. For a spheroid with hydrodynamic stick-boundary conditions[53,54],

$$[\eta]^{ell} = \frac{5}{2} + \frac{32}{15\pi}\left[\frac{b}{a}-1\right] - 0.628\left[\frac{1-a/b}{1-0.075a/b}\right], \tag{7}$$

which for $a = b$ reduces to the Einstein result, $[\eta]^{sph} = 2.5$, for a solid sphere. Note here that $[\eta]^{ell} > 2.5$ for $a \neq b$. Explicitly, $[\eta]^{ell} = 3.25$ for the best fit values a and b given in Figure 1. On demanding equality of the interaction-independent linear terms in the virial expansions of the viscosity,

$$\frac{\eta}{\eta_0} = 1 + [\eta]\phi + \mathcal{O}(\phi^2),$$

for spheroids and effective spheres, and on using $\phi^{ell} = (4\pi/3)ab^2n$ and $\phi^{sph} = (\pi/6)\sigma_{[\eta]}{}^3 n$ for an equal number density n, the effective diameter $\sigma_{[\eta]} = 7.42$ nm is obtained.

Due to the moderate aspect ratio, $b/a = 2.71$, the four obtained effective diameters are quite similar in magnitude. We use $\sigma = \sigma_{B_2} = 7.40$ nm in all our calculations of static and dynamic properties discussed in this paper.

Static scattering intensity and structure factor

Concentrated protein solutions exhibit pronounced interparticle correlations which are reflected in the static scattering intensity. This applies also to dilute, low-salinity solutions where the proteins show long-ranged electrostatic repulsion.

In order to allow for an analytical theoretical treatment, we assume that the static scattering intensity of interacting BSA proteins can be approximated by

$$I(q) = Ac_pP_{ell}(q)S_m(q), \tag{8}$$

where S_m is the so-called measurable static structure factor. Here, A is a q-independent factor (of dimension velocity^3), that should be the same for all intensity measurements corrected for recording time and source intensity.

For calculating $S_m(q)$, we use the rotational-translational decoupling approximation[37,55], where the spheroid shape is accounted for in the scattering amplitudes only, so that

$$S_m(q) = \Big[1 - X(q)\Big] + X(q)S(q). \tag{9}$$

Here,

$$X(q) = \frac{1}{P_{ell}(q)}\left[\int_0^1 d\mu\, f(q,\mu)\right]^2, \tag{10}$$

with $0 \le X(q) \le 1$ and $X(q\to 0) = 1$, and S is the so-called ideal structure factor of ideally monodisperse effective spheres of diameter $\sigma = \sigma_{B_2}$ and screened Coulomb repulsion of DLVO type. For the BSA model spheroid used here, $X(q)$ stays close to unity for $q \lesssim 0.5$ nm^{-1}, decaying for larger q steeply towards its first zero value at $q \approx 1.3$ nm^{-1}. For $q > 1.3$ nm^{-1}, $X(q) < 0.04$. The orientational disorder assumed in the decoupling approximation has the general effect of damping the oscillations in $S_m(q)$. While $S_m(q)$ is practically equal to one for $q \gtrsim 1.3$ nm^{-1}, irrespective of the still visible oscillations in $S(q)$, the effect of orientational disorder on $S_m(q)$ is weak in the range $q \lesssim 0.5$ nm^{-1}, where the most distinctive features in $S(q)$ are seen. We further note that $S_m(q\to 0) = S(q\to 0)$ for monodisperse systems, a feature which plays an important role in our upcoming discussion of collective diffusion.

The ideal structure factor, $S(q)$, entering into Eq. (9), is calculated using the repulsive part of the DLVO pair-potential[5],

$$\beta u(x) = \begin{cases} \infty, & x = r/\sigma < 1, \\ \gamma\dfrac{e^{-kx}}{x}, & x > 1, \end{cases} \tag{11}$$

also referred to as the hard-sphere Yukawa (HSY) potential. The coupling parameter, γ, and the screening parameter, k, are given by

$$\gamma = \frac{L_B}{\sigma}\left(\frac{e^{k/2}}{1+k/2}\right)^2 Z^2, \tag{12a}$$

$$k^2 = k_c^2 + k_s^2 = \frac{L_B/\sigma}{1-\phi}\left(24\phi|Z| + 8\pi n_s\sigma^3\right). \tag{12b}$$

Here, $L_B = \beta e^2/\varepsilon$ is the solvent-characteristic Bjerrum length in Gaussian units, $\beta = 1/(k_BT)$, ε is the solvent dielectric constant, and Z is the effective protein charge number in units of the proton elementary charge e. The factor $1/(1-\phi)$ in k^2 corrects for the free volume available to the microions[56,57]. We have not included van der Waals (vdW) forces in $u(x)$. However, we have checked that the influence of vdW attractions is small for most of the considered systems.

Eq. (12b) consists of two additive parts. The first part, $k_c^2 \propto |Z|$, is due to protein-surface released counterions, which are assumed to be monovalent. The second part, k_s^2, accounts for the screening due to all other monovalent microions. Owing to the overall charge neutrality, this contribution is proportional to the co-ion concentration n_s. A lower bound of $n_s \ge 10^{-7}$ M in pH-neutral aqueous solutions is due to the self-dissociation of water. Additional contributions to n_s can

arise from dissolved CO_2, and added salt such as NaCl. For a protein solution, n_s can have a (putatively linear) dependence on c_p if charged protein oligomers are present, acting as an additional source of surface-released counterions not contained in our model. Moreover, the protein stock solution might contain a residual amount of salt, and the proteins might dissociate acidic or alkaline surface groups during solvation. Note that due to the overall charge neutrality, the total concentration of monovalent counterions is given by $n_s + 6\phi|Z|/(\pi\sigma^3)$.

In recent work[6,7], two of the present authors have derived a computationally efficient integral equation scheme for computing $S(q)$ using the screened Coulomb potential in Eq. (11). This so-called modified penetrating background corrected rescaled mean spherical approximation (MPB-RMSA) shares the analytical simplicity of the widely used RMSA[46,58], but is distinctly more accurate. All calculations of $S(q)$ in this paper are based on the MPB-RMSA.

The spheroid-Yukawa (SY) model used in our calculations of $I(q)$ and $S_m(q)$ ignores orientational-translational coupling. Therefore, it can be expected to apply only to fluid-phase BSA solutions when c_p is sufficiently low, and when the ionic strength is not too large, so that the anisotropic protein shape and pair-interaction parts are not important. At larger c_p, there is orientational-translational coupling, and the decoupling approximation becomes invalid. We note again that the possible presence of residual protein oligomers and scattering impurities is not accounted for in our one-component model. The virtue of the SY model, however, is its analytical simplicity. The concentration range in which the SY model is applicable to BSA is examined in Sec. 4.

Since we use a spherically symmetric screened Coulomb plus hard-core pair potential for the protein-protein interactions, a short discussion of the neglected anisotropy in the electric double layer around a charged spheroid is in order here.

The mean electrostatic potential, $\Phi(r,\mu) = \sum_{l=0}^{\infty}\Phi_l(r)P_l(\mu)$, of a spheroid with a corresponding axisymmetric charge distribution immersed in an electrolyte solution includes in general higher-order multipoles with $l > 0$. Here, r is the distance of the spheroid center to the field point, $\mu = \cos\vartheta$ is the cosine of the angle relative to the spheroid rotational symmetry axis, and the P_l's are Legendre polynomials.

For large r, all multipoles decay asymptotically equally fast according to[59–64]

$$\Phi_l(r) \sim f_l \frac{e^{-\kappa r}}{r}, \tag{13}$$

where κ denotes the inverse electrostatic screening length, and f_l depends on the charge distribution. This implies that, in principle, the pair interaction energy of two spheroids depends on their relative orientation even when $r \gg \kappa^{-1}$. However, the multipolar strengths, f_l, for a spheroid with $b/a \sim 1$ can be expected to be small for larger l. Moreover, since after orientational averaging, $\langle P_l(\mu)\rangle_\mu = 0$ for all $l > 0$, our neglect of anisotropic pair interaction contributions can be expected to be reasonable, for systems where the particles can essentially rotate freely.

Short-time diffusion

We summarize here the analytical methods used in calculating the (short-time) collective diffusion coefficient d_C. These methods require $S(q)$ as their only input, with the BSA protein interactions described by the spherical pair potential in Eq. (11).

The colloidal short-time regime covers correlation times t within $\tau_B \ll t \ll \tau_I$. Here, $\tau_B = m_p/(3\pi\eta_0\sigma)$ is the momentum relaxation time of a globular protein of mass m_p. Within a short-time span, a protein has diffused a very small fraction of its size only. For BSA in water, $\tau_B \sim 1$ ps, and $\tau_I \approx 0.3$ μs. The BSA short-time dynamics is thus not resolved in our DLS experiment determining the measurable dynamic structure factor, $S_m(q,t)$, as a function of wavenumber q and correlation time t.

Within the translational-orientational decoupling approximation used in the SY model, $S_m(q,t)$ is determined as

$$S_m(q,t) = [1 - X(q)]\, G(q,t) + X(q) S(q,t), \tag{14}$$

where $G(q,t)$ and $S(q,t)$ are, respectively, the self intermediate scattering function[65], and the dynamic structure factor of ideally monodisperse, charged effective spheres interacting according to Eq. (11).

As discussed in relation to Eq. (3), the diffusion of oligomers or impurities results in a well-separated mode in $g_2(q,t)$, with a decay rate about ten times larger than $q^2 d_C^L$. Therefore, we denote the (monomeric) protein-protein dynamic structure factor, corrected for the well-separated slow oligomer mode, by $S_m^p(q,t)$.

Owing to the smallness of the proteins compared to the wavelength of visible laser light used in our DLS experiments, one obtains $t \gg \tau_I$ and $q \ll q_m$. Here, q_m is the wavenumber where S attains its principle peak value. On recalling that $X(q \ll q_m) \approx 1$, it follows that the influence of orientational disorder on $S_m^p(q,t)$ via the anisotropic spheroid scattering amplitude $f(q,\mu)$ is negligible. As a consequence,

$$S_m^p(q \ll q_m, t \gg \tau_I) \propto \exp\left[-q^2 d_C^L t\right]. \tag{15}$$

To calculate $d_C^L \approx d_C^S$, we use two complementary analytical methods, namely a self-part corrected version of the so-called $\delta\gamma$ scheme due to Beenakker and Mazur[8,66–69], denoted here as the corrected $\delta\gamma$ scheme for brevity, and a pairwise additive (PA) approximation of the HIs. The latter becomes exact at very low concentrations, but its prediction for d_C^S worsens

when protein volume fractions $\phi \gtrsim 0.05$ are considered (see our discussion of Figure 3 in Sec. 5). On the other hand, the PA predictions for η_∞, and for the short-time self-diffusion coefficient d_S not considered here, are reliable up to substantially larger volume fractions, as has been ascertained in comparison to Stokesian Dynamics computer simulations[8,26] and experimental data[66]. The PA expression for d_C^S reads

$$\begin{aligned}\frac{d_C^S}{d_0} &= \frac{1}{S(q\to 0)}\left\{\frac{d_S}{d_0} - 5\phi + 12\phi\int_1^\infty dx x[g(x)-1]\right.\\ &\quad +24\phi\int_1^\infty dx x^2 g(x)\tilde{y}_{12}^a(x)\\ &\quad \left.+\,8\phi\int_1^\infty dx x^2 g(x)\left[\tilde{x}_{12}^a(x)-\tilde{y}_{12}^a(x)\right]\right\}, \qquad (16)\end{aligned}$$

with d_S given in PA approximation by

$$\frac{d_S}{d_0} = 1 + 8\phi\int_1^\infty dx x^2 g(x)\left[x_{11}^a(x)+2y_{11}^a(x)-3\right]. \qquad (17)$$

The two-body mobility functions, x_{ij}^a and y_{ij}^a, can be expanded analytically in powers of $\sigma/r = 1/x$. The short-range mobility parts

$$\begin{aligned}\tilde{x}_{12}^a(x) &= x_{12}^a(x) - (3/4)x^{-1} + (1/8)x^{-3},\\ \tilde{y}_{12}^a(x) &= y_{12}^a(x) - (3/8)x^{-1} - (1/16)x^{-3},\end{aligned}$$

include all terms in the series expansion in $1/x$ with the far-field terms up to the dipolar level subtracted off. For $x > 3$, an explicit analytical expansion to $\mathcal{O}(x^{-20})$ is used[70]. Since the series expansion in $1/x$ converges slowly at small separations, accurate numerical tables, which account for lubrication at near-contact distances[71], are employed for $x < 3$.

The only input required in Eqs. (16) and (17) is the radial distribution function g, related to S by a one-dimensional Fourier transform[65]. The two functions are obtained in our analysis by the analytical MPB-RMSA.

The second short-time method used in the present work for calculating $d_C^S \approx d_C$ and η_∞, is the self-part corrected $\delta\gamma$ scheme. In this scheme, d_C^S is obtained from the exact relation[37]

$$\frac{d_C^S}{d_0}\lim_{q\to 0} S(q) = \frac{d_S}{d_0} + \lim_{q\to 0} H_d(q) \qquad (18)$$

containing the distinct part, $H_d(q)$, of the so-called hydrodynamic function $H(q)$. The $\delta\gamma$ scheme of Beenakker and Mazur provides an easy-to-use integral expression for $H_d(q)$, including $S(q)$ as the only required input. The explicit form of the $\delta\gamma$-scheme expression for $H_d(q)$ is given in[26,69] and will be thus not repeated here.

Extensive comparisons with Stokesian Dynamics simulations[8,26], and experiments on charged colloids[66,72], and for small ϕ also with PA calculations, have shown that the $\delta\gamma$ scheme predictions for $H_d(q)$ are good for all concentrations up to the freezing transition value, even though the $\delta\gamma$ scheme involves hydrodynamic approximations at any concentration. In particular, it disregards lubrication effects. Lubrication, however, is inconsequential for charge-stabilized particles where near-contact configurations are unlikely.

Different from $H_d(q)$, the accuracy of the $\delta\gamma$ scheme is less good for charged particles regarding the self-part, d_S, of d_C^S in Eq. (18)[26,66]. To remedy this deficiency, we use a hybrid method, referred to as the self-part corrected $\delta\gamma$ scheme, in which d_S is calculated using the PA expression in Eq. (17). It has been shown both for charged colloids[8,26,66] and Apoferritin protein solutions[73], that this hybrid method works well at fluid state concentrations.

High-frequency viscosity

The high-frequency viscosity, η_∞, linearly relates the average suspension shear stress to the average rate of strain in a low-amplitude, high-frequency oscillatory shear experiment. While this short-time quantity has been rather routinely determined for micron-sized charge-stabilized colloids[25,74], a direct mechanical measurement of η_∞ for BSA solutions is difficult, since the required frequencies $\omega \gg \tau_I^{-1}$ are in the MHz regime. We are interested here in η_∞ since, according to Eq. (1), it is an important contribution to the static viscosity η. The latter has been determined experimentally in the present work.

In PA approximation, η_∞ is given by[26,75,76]

$$\frac{\eta_\infty}{\eta_0} = 1 + \frac{5}{2}\phi(1+\phi) + 60\phi^2\int_1^\infty dx x^2 g(x) J(x), \qquad (19)$$

where the rapidly decaying shear mobility function $J(x)$, with $J(x) = 15/128\ x^{-6} + \mathcal{O}(x^{-8})$ for stick boundary conditions, accounts for two-body HI effects. In performing the integral over $g(x)$, the leading-order long-distance contribution is dominating for $x > 3$. Accurate numerical tables[71], where the lubrication effect for $x \approx 1$ is included, are used for $x < 3$.

The $\delta\gamma$ scheme of Beenakker and Mazur can be also used for calculating η_∞. Similar to the $\delta\gamma$-scheme expression for d_C^S, the standard (2^{nd} order) $\delta\gamma$ scheme result for η_∞ consists of a microstructure-independent self-part, and a distinct part given in form of an integral over $S(q)$[68]. In recent work, two of the present authors have shown that a self-part corrected version of the original $\delta\gamma$ scheme expression for η_∞ gives results for charged particles in very good agreement with Stokesian Dynamics simulations[8]. This self-part corrected $\delta\gamma$ scheme for η_∞ is used in the present work.

Static shear-viscosity

In long-time rheological measurements on protein solutions under steady shear, there is an additional shear-stress relax-

ation part, $\Delta\eta$, contributing to the static viscosity $\eta = \eta_\infty + \Delta\eta$. This contribution is influenced both by HIs and direct interaction forces. It can be calculated approximately within the mode-coupling theory (MCT) of Brownian systems. While a version of MCT for $\Delta\eta$ with far-field HI included has been discussed in earlier work together with an extension to multicomponent systems[77], for analytical simplicity we use here the standard one-component expression

$$\Delta\eta^{MCT} = \frac{k_B T}{60\pi^2}\int_0^\infty dt \int_0^\infty dq\, q^4 \left[\frac{S(q,t)}{S(q)}\frac{d}{dq}\log S(q)\right]^2, \quad (20)$$

which has been obtained, e.g. in[77], under the neglect of HIs. In principle, $\Delta\eta^{MCT}$ should be calculated self-consistently by a numerically expensive algorithm in combination with the corresponding MCT memory equation for $S(q,t)$[78]. However, the BSA solutions explored here are rather weakly coupled particle systems, with structure factor maxima $S(q_m) < 1.2$. Thus, as we have thoroughly checked in comparison to fully self-consistent MCT calculations, $\Delta\eta^{MCT}$ can be obtained more simply in a first iteration step where $S(q,t)$ in the integral of Eq. (20) is approximated by its short-time form $S(q,t)/S(q) = \exp[-q^2 d_0 t/S(q)]$, valid without HI. The difference to the fully self-consistent result for $\Delta\eta^{MCT}$ is at most a few percent, even for the most concentrated systems considered.

Moreover, again due to the only moderately strong interparticle correlations, $\Delta\eta$ augments η_∞ by at most ten percent. Therefore, the neglect of HI in $\Delta\eta^{MCT}$ can be expected to be rather insignificant for the systems considered since the dominant effect of HI is included already in η_∞. Theoretical results for η shown in this paper are all based on the first iteration solution for $\Delta\eta^{MCT}$, and on η_∞ calculated using the self-part corrected $\delta\gamma$ or PA schemes. For all explored systems, the difference in η_∞ between the PA and corrected $\delta\gamma$ scheme is at most two percent.

4 Static properties: experiment and theory

4.1 Form factor fit

In Figure 1, SAXS intensities for BSA solutions of very small protein weight concentrations, $c_p = 1$ and 2 mg/ml, and 150 mM of added NaCl, are shown along with the best-fit spheroid form factor. Note that our form factor fit relies on a simplified shape model, so that some controlled systematic deviations from experimental data are to be expected. To check for a residual effect of interparticle correlations on $I(q)$, $S(q)$ was calculated for the present two systems to first order in ϕ using the full DLVO potential, with $|Z| \sim 30$ and a Hamaker constant of $3k_BT$[79]. The so-obtained structure factor deviates only very little from unity with $S(q \to 0) \approx 0.99$.

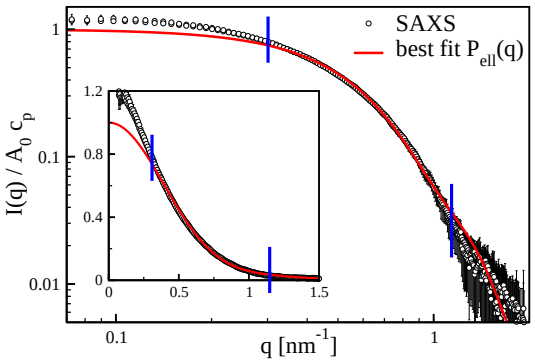

Figure 1 BSA form factor fit. Open circles: SAXS intensities at two protein concentrations of $c_p = 1$ and 2 g/l, for 150 mM of added NaCl. The SAXS intensities have been divided by c_p, and by a common, q-independent factor A_0. Red solid line: Angular-averaged spheroid form factor according to Eq. (4), fitted to the SAXS data within 0.3 nm$^{-1} < q <$ 1.15 nm^{-1}, as indicated by the blue vertical line segments. The obtained fit values are $a = 1.75$ nm and $b = 4.74$ nm. Inset: Intensity on a double linear scale.

Thus, to fit the measured intensity in Figure 1, we have used Eq. (8) for $I(q)$ with $S_m(q)$ set equal to one. Using an automatic weighted least-squares minimizer, the spheroid semi-axes a and b entering into $P_{ell}(q)$ were varied to achieve a best fit intensity for a given prefactor A in Eq. (8). This fitting procedure was iterated for different values for A, until optimal agreement with the SAXS intensities within the range 0.3 nm$^{-1} < q <$ 1.15 nm^{-1} was achieved, resulting in $a = 1.75$ nm and $b = 4.74$ nm. These values for the spheroid semi-axes are in good accord with previously reported values, and in reasonable agreement with the linear dimensions of the reported heart-shape like crystal structure of albumins[42–44,46]. In a related, recent study by part of the present authors[17], similar values $a = 1.80 \pm 0.05$ nm and $b = 4.60 \pm 0.15$ nm have been determined, which are in decent agreement with the values obtained here. The optimized value for A, denoted by A_0, has been also used in our SAXS intensity fits for systems without added salt, which will be discussed in the following subsection.

The best-fit form factor, P_{ell}, depicted in Figure 1 deviates from the SAXS intensities outside the fitted q-range. For $q \gtrsim 1.15$ nm^{-1}, corresponding to length scales $2\pi/q \lesssim 6$ nm $\lesssim \sigma$, the complex internal structure of BSA is probed, which is not accounted for in our simplifying SY model. The deviations visible for $q \lesssim 0.3$ nm^{-1}, corresponding to distances of roughly 20 nm or larger, are likely due to additional scattering species made up of larger particles such as BSA oligomers or impurities. Since the size-, form-, and charge-distributions of oligomers and impurities are unknown, our choice of the lower q-boundary in fitting $I(q)$ is somewhat more ambiguous than

the upper boundary. Therefore, we have repeated the intensity fitting for various low-q boundaries, finding that the weighted least squares deviation increases dramatically if the boundary is selected below 0.3 nm^{-1}. Moreover, the fit values for a and b remain essentially constant when the lower q-boundary is chosen larger than 0.3 nm^{-1}.

The fit parameters of a spheroid form factor to SAXS data of proteins in general depend slightly on the measured q range, the prepared protein concentration, solvent and salt conditions, and background subtraction. In the context of the present study, the related changes of the spheroid model parameters are small compared to the experimental error bars and will be discussed in the next section.

4.2 Concentration series of scattered intensities

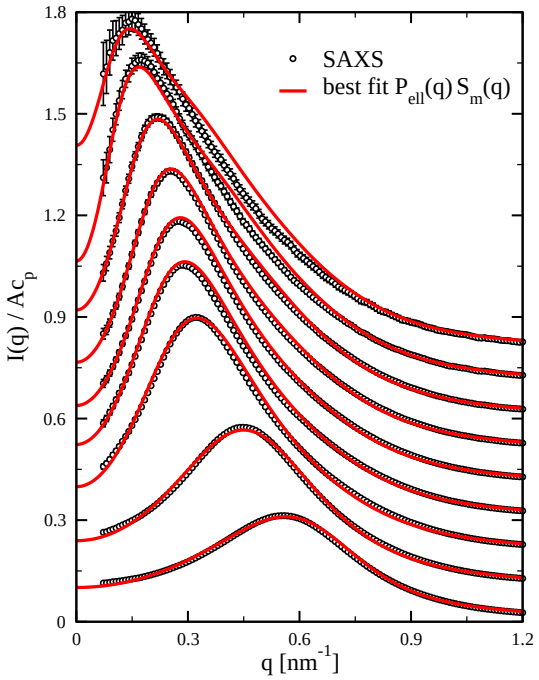

Figure 2 SAXS intensities from BSA solutions at various c_p, without added salt, divided by Ac_p. From top to bottom: $c_p = 0.9, 1.8, 4.5, 7.2, 9, 13.5, 18, 45$, and 90 mg/ml. The intensity curves are displaced in steps of 0.1 along the vertical axis for better visibility. The SAXS-data for the extended range $q \lesssim 4$ nm^{-1} were taken into account in all fits, but shown here only up to $q = 1.2$ nm^{-1}. Red solid lines: best fits according to Eq. (8) with $S(q)$ calculated in MPB-RMSA. The fit parameters are listed in Table 1.

Figure 2 includes the SAXS intensities for all explored BSA solutions without added salt that could be fitted using the decoupling approximation expression in Eq. (8), for $S(q)$ calculated in MPB-RMSA using the screened Coulomb potential in Eq. (11). In order to emphasize the shape differences across the data set, the intensities are divided by their respective fitted amplitudes A, and by the protein concentrations c_p. The most concentrated solution shown here is the one for $c_p = 90$ mg/ml. Two even more concentrated systems for $c_p = 180$ and 270 mg/ml are not depicted in the figure since their intensities could not be fitted reasonably well by the SY model.

Table 1 Fit parameters ϕ, $|Z|$, n_s, and A/A_0, for the BSA concentration series without added NaCl, with intensities shown in Figure 2. The additional parameters $L_B = 0.711$ nm, $\sigma = \sigma_{B_2} = 7.40$ nm, $a = 1.75$ nm, $b = 4.74$ nm are kept fixed, and A_0 is taken from the form factor fit in Figure 1. The obtained fit values at $c_p = 0.9, 1.8, 45$, and 90 mg/ml should be taken with a pinch of salt (see related text). The listed values for c_p are according to Eq. (2).

c_p [mg/ml]	ϕ	$\|Z\|$	n_s [μM]	A/A_0
0.9	5.19×10^{-4}	34.5	1216	1.20
1.8	1.34×10^{-3}	18.8	608	1.08
4.5	3.72×10^{-3}	19.1	1278	0.96
7.2	6.97×10^{-3}	16.7	1497	0.97
9	1.04×10^{-2}	14.6	1510	1.05
13.5	1.28×10^{-2}	12.6	1297	0.81
18	2.06×10^{-2}	10.8	1292	0.85
45	8.19×10^{-2}	9.47	2375	1.0
90	1.74×10^{-1}	8.52	3323	1.0

In order to fit the experimental intensity data using Eq. (8), some deviations of the prefactor A from the optimized form factor fit value A_0 have to be allowed for (see Table 1). The fit of each individual intensity curve in Figure 2 was made as follows: After dividing the SAXS intensity by A_0 and c_p, the weighted sum of quadratic deviations between SAXS data points and the intensity according to Eq. (8) was minimized by an automatic three-dimensional weighted least-squares minimizer with respect to the fitting parameters $\{|Z|, n_s, \phi\}$. For each concentration, the whole experimental data set was used, for wavenumbers from 0.07 to about 4 nm^{-1}. If the fit was unsatisfactory, the prefactor A was slightly altered, and the optimization with respect to $\{|Z|, n_s, \phi\}$ was repeated. This procedure was iterated until convergence in all fit parameters was achieved. For all considered concentrations, $L_B = 0.711$ nm, $\sigma = \sigma_{B_2} = 7.40$ nm, $a = 1.75$ nm, and $b = 4.74$ nm were kept fixed. Table 1 summarizes the obtained best fit parameters.

While the overall intensity fits for the two lowest concentrations, $c_p = 0.9$ and 1.8 mg/ml, look reasonably good, they contain some peculiarities. A shoulder is present in the fit intensity extending from $q \approx 0.3$ to 0.8 nm^{-1}, overshooting the

experimental data by several standard deviations. Moreover, the prefactor A is substantially larger than A_0 in both cases, and the fitted effective charge number $|Z|$ assumes a questionably large value of 34.5 for $c_p = 0.9$ mg/ml. These peculiarities can be attributed to impurity contributions neglected in Eq. (8). Note that the maximal intensities in both systems occur at wavenumbers well below the value 0.3 nm^{-1}, where impurities are found to obstruct also the form factor fit in Figure 1.

All our attempts to remedy these fitting problems for the two most dilute samples failed. Lacking information about the shape and size distribution, and the interactions of the impurities, we cannot improve on Eq. (8). Restricting the wavenumber interval in the fitting procedure to $q \gtrsim 0.3$ nm^{-1} leads to no improvement, either. While Eq. (8) is expected to be accurate in this restricted q-range, the maximum in $I(q)$ is not included. The intensity for $q > 0.3$ nm^{-1} is a monotonically decaying curve, almost completely determined by the form factor. It therefore lacks distinct features coming from particle correlations, rendering the fit with respect to $\{|Z|, n_s, \phi\}$ into an overdetermined problem. For all these reasons, our fit parameters in Table 1 for $c_p = 0.9$ and 1.8 mg/ml should not be considered as quantitatively accurate.

Except for the two most dilute systems, all other systems with concentrations from $c_p = 4.5$ to 90 mg/ml included in Figure 2 can be excellently fitted by Eq. (8). The obtained effective charges, salt concentrations, and volume fractions all assume reasonable values, showing systematic dependencies on the BSA concentration. Note, however, that for $c_p = 45$ and 90 mg/ml, the SY model is pushed to its limit. On assuming a Hamaker constant of 3 k_BT [79], the repulsive barrier height of the DLVO potential becomes very small, with values of 1.3 and 0.5 k_BT at $c_p = 45$ and 90 mg/ml, respectively. The contact value of $g(x)$ at $x = 1$ is just barely zero for the more dilute system, whereas $g(x = 1^+) \approx 0.9$ in the more concentrated system. Obviously, the SY model with purely repulsive, spherically symmetric pair interactions is bound to fail when the particles are allowed to come into hard-core contact. Thus, the system with $c_p = 45$ mg/ml, and fitted volume fraction $\phi = 8.19\%$, is clearly on the borderline of the SY model. Somewhat unexpectedly, and probably fortuitously, the system with $c_p = 90$ mg/ml can still be fitted with good accuracy. Summarizing, the fit values for the most concentrated systems with $c_p = 45$ and 90 mg/ml in Table 1 should be interpreted with caution, since the fit parameters might be significantly distorted by the discussed deficiencies of the SY model. An indication for this could be the obtained fit values for $\phi(c_p)$, which for the two most concentrated samples clearly overshoot the linear dependence on c_p found approximately for the lesser concentrated systems (see Table 1).

In closing our discussion of the static scattered intensities, we note that fit parameters slightly different from the ones in Table 1 are obtained, when in place of the BSA model spheroid axes $(a,b) = (1.75\text{ nm}, 4.74\text{ nm})$, the values $(a,b) = (1.80\text{ nm}, 4.60\text{ nm})$ given in [17] are used. For instance, at $c_p = 4.5$ and 18 mg/ml, the best-fit values for $|Z|$ change to 18.4 and 10.7, respectively. Note that, in comparison to [46], where the RMSA was employed in fitting $I(q)$, we use here the improved MPB-RMSA integral equation scheme for $S(q)$, resulting in more precise fit-values. Moreover, different from the earlier intensity fitting described in [46], the dephasing influence on $I(q)$ originating from the particle asphericity is accounted for approximately in the decoupling approximation used in the present study. The slightly different spheroid semi-axes $(a,b) = (1.80\text{ nm}, 4.60\text{ nm})$, and the corresponding, slightly changed fit-parameters, do not cause appreciable changes in the dynamical properties. For instance, the collective diffusion coefficient changes by no more than 3%, and the changes in the static- and high-frequency viscosities are less than 0.1%. Note that the somewhat smaller spheroid causes changes of the fitted volume fraction of about 5% which does not change absolute values but slightly rescales the protein concentration axis for the theoretical predictions.

5 Dynamic properties: experiment and theory

In the following, we compare the DLS data for the collective diffusion coefficient of BSA solutions, and the static shear viscosity measured in our suspended Couette-type rheometer, to the results of the dynamic schemes discussed in Sec. 3. Moreover, we assess the accuracy of a generalized Stokes-Einstein relation connecting the viscosity to the collective diffusion coefficient and the isothermal osmotic compressibility. We reemphasize here that the employed theoretical schemes use $S(q)$ and $g(r)$ as the only input. With $S(q)$ and $g(r)$ determined from the fits to the SAXS-intensities, all theoretical results for d_C, η_∞ and η are thus obtained without any additional adjustable parameters.

5.1 Collective diffusion coefficient

Figure 3 includes our SLS/DLS data for $1/S(q \to 0)$ (upper part) and $d_C^L = d_C$ (lower part), for aqueous BSA solutions in comparison with the theoretical predictions. Systems without added salt, and for concentrations $n_s = 5$ and 150 mM of added NaCl, are considered. Additional measurements using 500 mM of added NaCl (data not shown) agree almost perfectly with the data for $n_s = 150$ mM, indicating that electrostatic repulsion is fully screened already at $n_s = 150$ mM. As the input to the dynamics schemes, $S(q)$ and $g(r)$ were generated by the MPB-RMSA, using concentration-interpolated input parameters $\phi(c_p)$ and $Z(c_p)$ based on Table 1. For no added salt, $n_s(c_p)$ was interpolated using Table 1, while $n_s = 5$ and 150

mM were kept fixed (independent of c_p) in the corresponding theoretical calculations. The value $d_0^{ell} = 5.82$ Å^2/ns of the spheroid translational free diffusion coefficient was used to obtain d_C in the experimental units from the dimensionless results for d_C/d_0 obtained by both theoretical schemes.

For no added salt, the experimental $d_C(c_p)$ assumes a maximum at $c_p \approx 10-20$ mg/ml. This maximum is qualitatively reproduced by both theoretical schemes (corrected $\delta\gamma$ and PA), but its location is predicted to occur at somewhat larger concentrations $c_p \approx 20-30$ mg/ml. For BSA concentrations larger than the concentration at the maximum value for d_C, the PA-predicted $d_C(c_p)$ reduces strongly, eventually reaching non-physical negative values for $c_p \gtrsim 110$ mg/ml. This illustrates the expected failure of the PA scheme at higher concentrations, indicating that three-body contributions to HI, totally left out in the PA, but not in the $\delta\gamma$ scheme, come into play for $c_p \gtrsim 30$ mg/ml. Up to the concentration value at the maximum of d_C, both schemes agree very well, with residual differences not visible for $c_p \lesssim 20$ mg/ml on the scale of Figure 3. Despite its residual small inaccuracies, the self-part corrected $\delta\gamma$ expansion will therefore be used in the following calculations of d_C.

The physical origin of the non-monotonous concentration dependence $d_C(c_p)$ at low concentrations of salt can be understood on the basis of Eq. (16), rewritten using $d_C \approx d_C^S$ as

$$\frac{d_C}{d_0} = \lim_{q\to 0} \frac{H(q)}{S(q)}, \qquad (21)$$

with $H(q) = d_s/d_0 + H_d(q)$. The ratio in Eq. (21) consists of two competing factors. The factor $1/S(q\to 0)$, inversely proportional to the isothermal osmotic compressibility of ideally monodisperse particles, increases monotonically as a function of the BSA concentration. Owing to the larger coupling constant γ in Eq. (12a), a much steeper initial increase of $1/S(q\to 0)$ is observed for weakly screened systems than for systems with added salt (c.f. the top panel of Figure 3). As c_p is further increased, the amount of surface-released counterions increases correspondingly, leading to an enhanced electrostatic screening. As a consequence, the rate of change of $1/S(q\to 0)$ with c_p reduces significantly at a colloid concentration roughly set by the criterion, $k_c^2(c_p) = k_s^2$, of equal surface released counterion and salt-co-ion contributions to the screening parameter in Eq. (12b).

The nominator in Eq. (21) is the reduced sedimentation velocity, $H(q\to 0)$, which is known from theory and experiment[66] to decrease monotonically, for not too large concentrations and low salinity according to $1 - a_{sed}\ \phi^{1/3}$, with $a_{sed} = 1.6\ -\ 1.8$ in the case of highly charged particles, and as $1 - 6.546\,\phi + 21.918\,\phi^2 + \mathcal{O}(\phi^3)$ for neutral hard spheres[80]. For strongly correlated particles, the competition between decreasing compressibility and decreasing sedimentation coeffi-

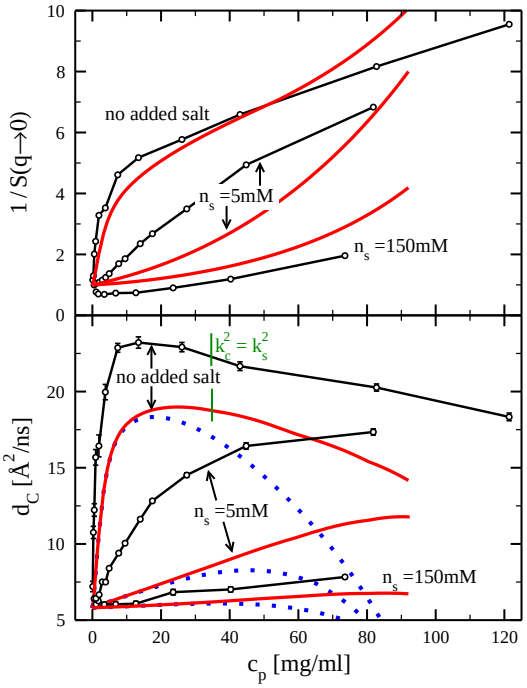

Figure 3 Top panel: Inverse zero-wavenumber limiting static structure factor of BSA solutions, obtained from SLS (connected black circles) and our MPB-RMSA scheme (red solid lines). Number concentrations, n_s, of added NaCl as indicated. Bottom panel: Fast mode coefficient, $D_1 = d_C^L$, obtained from the discussed double-exponential fit to the DLS data of BSA solutions (connected black circles), and d_C^S calculated by the self-part corrected $\delta\gamma$ scheme (red solid lines), and the PA approximation (blue dotted curves). All theoretical curves are based on input parameters $\phi(c_p)$ and $Z(c_p)$ interpolated from Table 1. In the zero added-salt case, the $n_s(c_p)$ values were also interpolated using Table 1. Theoretical results for added NaCl are obtained using fixed salt concentrations of $n_s = 5$ and 150 mM. The input parameters $L_B = 0.711$ nm, $\sigma = \sigma_{B_2} = 7.40$ nm, $a = 1.75$ nm, $b = 4.74$ nm, and $d_0 = d_0^{ell}(a,b) = 5.82$ Å^2/ns are kept fixed throughout. For the zero added-salt case, the green vertical line segment at $c_p \approx 34$ mg/ml marks the protein mass-concentration where the surface-released counterion contribution to k^2 in Eq. (12b) is equal to the coion contribution.

cient with increasing c_p leads thus to a maximum in $d_C(c_p)$, at a concentration roughly determined from $k_c^2(c_p) = k_s^2$.

The DLS-measured values for d_C are not quantitatively reproduced by the self-part corrected $\delta\gamma$ scheme. Both in the zero added-salt case, and for $n_s = 150$ mM, d_C is underestimated by the corrected $\delta\gamma$ scheme prediction by about 25%. The difference might be simply due to the complex-shaped BSA proteins having a translational free diffusion coefficient larger than the value $d_0^{ell} = 5.82$ Å^2/ns used in the SY model. In fact, an extrapolation of the experimental data for d_C to zero concentration leads to a larger value for d_0 in the range of $6-7$ Å^2/ns, which can completely explain the differences in d_C between experiment and theory. However, this low-concentration extrapolation should not be over-interpreted as being conclusive, since the experimental data are rather noisy for low concentrations.

While the agreement between the theoretical and the experimental d_C's is overall rather satisfying for very low and very high salt content, strong differences are found for the intermediate added NaCl concentration of 5 mM. This is not surprising, however, since already the zero added-salt experiments led to fit values for n_s of 1 to 3 mM. Therefore, n_s is most probably a function of c_p also in the 5 mM added NaCl case, instead of being constant as assumed in the calculations. Moreover, there is no obvious reason to expect that the relation $Z(c_p)$, interpolated from Table 1, remains valid at arbitrary added salt concentrations. Additional future SAXS measurements at 5 mM added NaCl are necessary to determine, for this case, the precise dependence of n_s and Z on c_p.

5.2 Static viscosity

The rheometric results for η without added salt, and with 150 mM of added NaCl, are plotted in Figure 4 as a function of c_p, and compared to the theoretical predictions. Apart from pronounced differences at lower concentrations, discussed in detail further down, the experimental data agree overall decently well with the theoretical predictions. Due to the rather weak microstructural ordering of the BSA proteins, characterized by structure factor peak heights less than 1.2 even for the most concentrated samples, the shear-stress relaxation term $\Delta\eta$ contributes only little to η, with a maximum relative contribution of about 10% near $c_p = 100$ mg/ml. The dominant contribution to η is given by η_∞, which is predicted to good accuracy both by the PA scheme and the corrected $\delta\gamma$ scheme, with practically equal results. The PA scheme is applicable to the whole experimentally probed concentration range of $c_p \lesssim 100$ mg/ml, since three-body and higher order HI contributions affect η_∞ to a lesser extent than d_C (c.f. here Fig. 3, showing the failure of the PA prediction for d_C already for $c_p \lesssim 50$ g/l).

The addition of larger amounts of salt lowers the values for

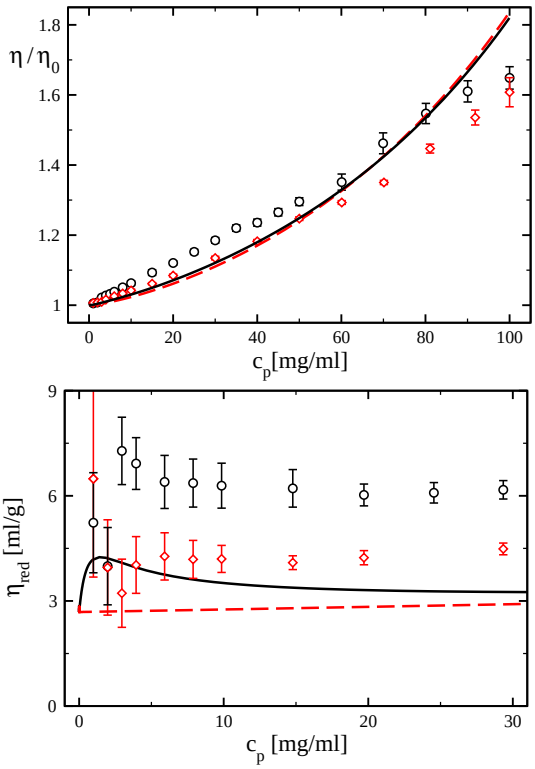

Figure 4 Static relative (top panel) and reduced (bottom panel) viscosity for $T = 25°$ C as function of c_p. Theoretical curves are based on input parameters $\phi(c_p)$ and $Z(c_p)$, concentration-interpolated using Table 1. Symbols: experimental data without added salt (black circles) and with $n_s = 150$ mM (red diamonds). Lines: theoretical results without added salt (black solid line, $n_s(c_p)$ interpolated using Table 1) and with a fixed salt concentration of $n_s = 150$ mM (red dashed curve). Note the different c_p-ranges in the two panels of the figure.

η, as can be noticed from the two experimental data sets depicted in Figure 4. The reason for this is the enhanced electrostatic screening, causing $\Delta\eta$ to decrease with increasing salinity in going from strongly structured, charged spheres to basically neutral hard spheres. In contrast, η_∞ is known from theory and experiment[8,26] to *increase* upon the addition of salt, due to the enlarged influence of near-field HIs when the particles are allowed to get closer to each other in electrostatically screened systems. Thus, η_∞ and $\Delta\eta$ have opposite trends in their dependencies on the concentration of added salt. These competing trends are the reason for the weak crossover in the two theoretical curves for η, noticed in the top panel of Figure 4 at $c_p \approx 67$ mg/ml. For particle concentrations larger than this c_p value, the increase of η_∞ overcompensates the decrease in $\Delta\eta$ when, in place of the zero added-salt system, a system with $n_s = 150$ mM is considered. That such a weak crossover is not observed in the experiment data in Figure 4, points to an underestimation of the crossover concentration by our simplifying theories for η, possibly due to the neglect of HIs in the $\Delta\eta$ calculation.

A remarkable feature is noticed from the bottom panel of Figure 4, where we plot the so-called reduced viscosity,

$$\eta_{red}(c_p) = \frac{\eta(c_p) - \eta_0}{\eta_0 c_p}, \tag{22}$$

as a function of c_p. The concentration-dependent function $c_p\eta_{red}/\phi$ reduces to the intrinsic viscosity, $[\eta]$, defined in Eq. (6), in the limit of vanishing concentration. The single-particle property $[\eta]$ is a viscometric measure of the particle non-sphericity. Note here that features of dilute systems are more clearly revealed in η_{red} than in η.

Both experimental data sets in the bottom panel of Figure 4 show a local maximum of η_{red} at low c_p values, which for the zero added-salt system (black open circles) is visible as a weak non-monotonicity near $c_p \approx 3$ mg/ml. For the system with 150 mM added NaCl (red open diamonds), the experimental maximum is represented essentially by a single data point at $c_p = 1$ mg/ml, where $\eta_{red} \approx 6.5$ ml/g, whereas the remaining data points describe a nearly constant plateau value of 4.5 ml/g. This plateau value is in good overall agreement with reported values for η_{red} at low c_p, in the range of 3.8 to 4.9 ml/g [12,81–83].

Regarding the large experiment error bars at very low c_p, from the figure, we can not attribute physical significance to the single-point maximum in the $n_s = 150$ mM system. A more refined data resolution in a future experimental study is clearly needed here. Even the maximum in η_{red} for the zero added-salt case might be disputable on basis of the experimental data alone. However, the existence of such a maximum in η_{red} draws its credibility from the comparison to the theoretical results, showing a maximum in $\eta_{red}(c_p)$ at a slightly lower value of c_p. A similar non-monotonic behavior of $\eta_{red}(c_p)$, with a pronounced peak at low c_p, has been measured also in polyelectrolyte systems[84–86], in low-salinity suspensions of charged silica spheres[87], and in microgels[88]. The effect has been described theoretically by scaling arguments[89], by the Rice-Kirkwood equation[90] for the shear viscosity in combination with a screened Coulomb potential[91], and for rod-like particles using a MCT scheme similar to ours[92]. In these earlier treatments, HI has been disregarded altogether. In our approach, HI is included in the for the present systems dominating η_∞ part of η.

To rule out that the non-monotonicity of the theoretical $\eta_{red}(c_p)$ is caused by BSA-specific dependencies of $|Z|$ and n_s on c_p, (c.f. Table 1), we have investigated additionally a purely theoretical HSY model system for fixed $|Z| = 20$ and $n_s = 1$ mM. Here, we find again a maximum in $\eta_{red}(c_p)$. Thus, the maximum in $\eta_{red}(c_p)$ is a generic effect in weakly screened HSY fluids. It is entirely due to the shear-stress relaxation term $\Delta\eta$, for $(\eta_\infty - \eta_0)/(\eta_0 c_p)$ increases monotonically in c_p at arbitrary salt concentration. Since the HIs are neglected in our MCT treatment of the shear-stress relaxation part $\Delta\eta$, we conclude that the local maximum in η_{red} is basically a non-hydrodynamic effect, arising from electrostatic repulsion. We point out that the discussed physical mechanism underlying the non-monotonic behavior of $\eta_{red}(c_p)$ is different from the one causing the maximum in d_C as a function of c_p. The latter maximum originates from a competition between electrostatic repulsion and hydrodynamic slowing in crowded systems. It is therefore not surprising that the maxima in η_{red} and d_C are located at considerably different protein concentrations. Whereas the maximum of d_C occurs at $c_p \approx 30$ mg/ml (c.f. Figure 3), the maximum in η_{red} is observed at $c_p \lesssim 5$ mg/ml.

The theoretical values for η_{red} in Figure 4 underestimate the experimental data by a factor of about $1/2$. In the low-concentration regime, the theoretical result for $\eta_{red}c_p/\phi$ approaches $[\eta] = 2.5$, owing to the underlying effective sphere model. The intrinsic viscosity of BSA modeled as a spheroid is $[\eta]^{ell} = 3.25$, which is larger than the value for a sphere by a factor of 1.3 only. Therefore, this can not be the only cause for the observed deviation. However, the actual intrinsic viscosity of a heart-like shaped BSA protein is neither equal to that of a spheroid nor to that of an effective sphere. We recall here our discussion of Figure 3, where we argued that d_0 for a BSA protein might well be about 25% larger than the free diffusion coefficient, d_0^{ell}, of the model spheroid. We can similarly argue that the observed differences between the experimental and theoretical η_{red} may be largely due to a value for the intrinsic viscosity of BSA of about $4-5$, which is $20-50\%$ larger than $[\eta]^{ell}$, and about twice as large as the $[\eta]$ value of spheres. This could explain the observed difference.

We note here that electrokinetic contributions to η, d_C, and to the long-time self-diffusion coefficient d_S, originating from

the non-instantaneous response of the microion-clouds around each protein, are not included in our theoretical treatment. Microion electrokinetics has the effect of lowering somewhat the values of d_C and d_S[73,93], while enlarging the viscosity η[94,95]. These effects can be expected to be stronger when κ^{-1} is approximately equal to the particle radius. Electrokinetic contributions to d_S have been shown to be less significant at higher macroion (protein) concentrations[96,97].

The slowing electrokinetic effect on d_C can be very roughly estimated on basis of the so-called coupled mode theory (CMT), which has been applied, e.g., to peptide solutions by Egelhaaf et al.[98], to lysozyme solutions by Retailleau et al.[93], and to apoferritin protein solutions by Gapinski et al.[73]. The work by Gapinski et al. includes a thorough theoretical discussion of the assumptions and approximations going into CMT, and it is outlined how this method can be improved in future work. Using the CMT expression in Eqs. (21-23) of Ref.[73] for d_c, we find that $d_C(c_p)$ is electrokinetically reduced by 6%, 10%, and 5%, at $c_p = 0.9$ mg/ml, 18 mg/ml, and 90 mg/ml, respectively. The respective values for the added salt concentration and protein effective charge entering into the CMT electrokinetic correction to d_C are taken from Table 1. The microionic Stokes-Einstein free diffusion coefficient appearing in the CMT expression was set qual to 1.45×10^2 Å^2/ns, corresponding to a microion radius of 1.5 Å. For the free diffusion coefficient of BSA, the ellipsoid value of 5.82 Å^2/ns was used. The electrokinetic reduction of d_C is thus rather weak for the considered BSA solutions.

5.3 Relation between viscosity and collective diffusion

Kholodenko and Douglas[28] have proposed the approximate generalized Stokes-Einstein (GSE) relation

$$\frac{d_C(\phi)\eta(\phi)}{d_0\eta_0}\sqrt{S(q\to 0,\phi)} \approx 1, \qquad (23)$$

between collective diffusion coefficient, (static) viscosity and the square-root of the isothermal osmotic compressibility coefficient $S(q\to 0,\phi)$. If this relation were exactly valid, the dimensionless function on the left-hand-side (lhs) of Eq. (23) would be a constant equal to one. The (approximate) validity of a GSE relation is very useful from an experimental viewpoint, since it allows to infer viscoelastic properties such as η_∞ and η from a dynamic scattering experiment where diffusion coefficients are determined. This is of particular relevance when the amount of protein available is too small for a mechanical rheometer measurement. Since we have experimental data sets for η, d_C, and $S(q\to 0)$ for BSA solutions with low and high salt content at our disposal, together with theoretical tools to calculate these properties, we are in the position to scrutinize the accuracy of the KD-GSE relation. We can do this not only for the special case of BSA solutions,

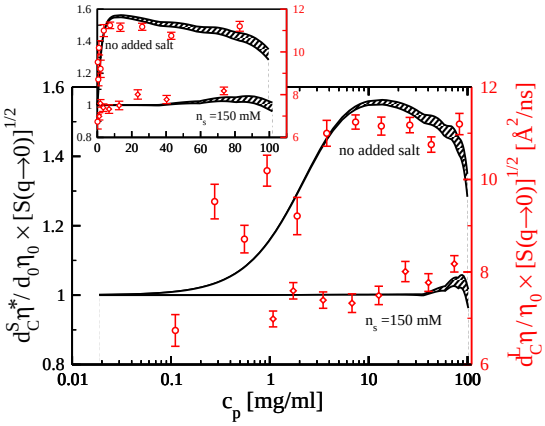

Figure 5 Test of the long-time and short-time KD-GSE relations in Eq. (23), with $\eta^* = \eta$ and $\eta^* = \eta_\infty$, respectively. Results for BSA solutions without added salt (upper data sets), and with 150 mM of added NaCl (lower data sets) are shown. Red symbols: combination of d_C^L from DLS, η/η_0 from suspended Couette rheometry, and $S(q\to 0)$ from SLS. Black lines: Theoretical results, combining $d_C^S \approx d_C^L$ and η_∞ calculated from the self-part corrected $\delta\gamma$ scheme with $S(q\to 0)$ from the MPB-RMSA scheme. For the long-time GSE version, $\eta = \eta_\infty + \Delta\eta$, with $\Delta\eta$ from MCT is used. Lower boundaries of the theoretical curves correspond to the short-time GSE, upper boundaries to the long-time version. The theoretical curves are based on $S(q)$-input with $\phi(c_p)$ and $Z(c_p)$ concentration-interpolated using Table 1. For zero added salt, $n_s(c_p)$ was also interpolated on basis of Table 1. The parameters $L_B = 0.711$ nm and $\sigma = \sigma_{B_2} = 7.40$ nm are kept fixed.

but with our theoretical methods more generally for arbitrary spherical colloidal particles interacting by the HSY potential in Eq. (11).

In their discussion of the GSE relation in Eq. (23), based on mode-coupling theory like arguments, Kholodenko and Douglas have considered explicitly a dilute suspension of colloidal hard spheres to first order in ϕ only, where η_∞ and η are identical, since $\Delta\eta = \mathcal{O}(\phi^2)$. For high concentrations, we test now the accuracy of both the long-time and short-time versions of the KD-GSE relation, on recalling that different from η_∞ and η, d_C^S and d_C^L are practically equal even at high concentrations. In Ref.[28], it was argued that for uncharged hard spheres (HS) the KD-GSE relation is valid to linear order in ϕ. We can check this statement analytically using numerically precise 2$^{\text{nd}}$ order virial expansion results for $d_C^{HS} = (d_C^S)^{HS}$, η_∞^{HS}, η^{HS}[80,99,100], and with $S^{HS}(q\to 0,\phi)$ calculated from the precise Carnahan-Starling equation of state. In this way,

we obtain

$$\frac{d_C^{HS}\eta_\infty^{HS}}{d_0\eta_0}\sqrt{S^{HS}(q\to 0)} = 1-0.046\phi+1.3713\phi^2+\mathcal{O}(\phi^3), \quad (24a)$$

$$\frac{d_C^{HS}\eta^{HS}}{d_0\eta_0}\sqrt{S^{HS}(q\to 0)} = 1-0.046\phi+2.282\phi^2+\mathcal{O}(\phi^3). \quad (24b)$$

The short- and long-time versions of the KD-GSE relation for hard spheres are identical to linear order in ϕ, with a coefficient, -0.046, which is not precisely vanishing but close to zero. However, to quadratic order in ϕ already, where particle correlations come into play and η_∞ needs to be distinguished from η, both GSE variants have distinctly non-zero virial coefficients. Since precise values for the higher-order virial coefficients are not known to date, an assessment of the accuracy of Eq. (23) for larger ϕ can be made only using simulation and experimental data for $d_C(\phi)$, $\eta_\infty(\phi)$ and $\eta(\phi)$. This assessment has been performed in[8], where it is shown that for neutral hard spheres, both variants of the KD-GSE relation apply decently well for $\phi \lesssim 0.3$.

It still remains to be investigated in which concentration range the two KD-GSE relations are significantly violated when, instead of neutral hard spheres, weakly screened, charged HSY-like particles such as charged proteins are considered. Note here that a virial expansion cannot be reasonably applied to charged particles at lower salinity, since the pair structure functions and thermodynamic properties in these systems depend on ϕ, γ and k in a non-analytical way.

In Figure 5, we plot the left-hand-side function in Eq. (23), both in its short- and long-time form, as a function of c_p. Both BSA solutions without added salt, and solutions with $n_s = 150$ mM are considered. Apart from a constant factor, which is related to the actual value of d_0 in BSA solutions discussed earlier, the theoretical curves compare reasonably well to the experimental data. There are only small differences in the short-time and long-time GSE curves in the case of BSA solutions.

With the hard-sphere-like behavior of the particles practically reached for $n_s = 150$ mM, in the added-salt system the two KD-GSE variants apply for concentrations up to $c_p \approx 50$ mg/ml, corresponding to $\phi \approx 0.1$. For more concentrated systems, the lhs function in Eq. (23) increases initially, going trough a shallow maximum near $c_p \approx 90$ mg/ml. For zero added salt, violation of the KD-GSE relations is observed theoretically at all non-zero concentrations, and can be noticed in our experiment already for $c_p \lesssim 1$ mg/ml.

In our discussion of the KD-GSE relation, we proceed now by characterizing the crossover behavior in going from the low-salt to the high-salt regime. To this end, in Figure 6, we plot the lhs of Eq. (23) as a function of ϕ for various salt contents, using the parameters $L_B = 0.711$ nm, $\sigma = 7.40$ nm, and

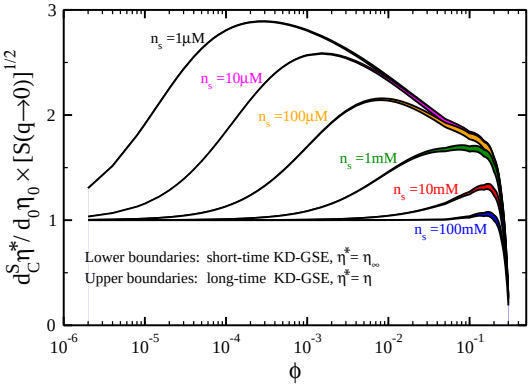

Figure 6 Accuracy assessment of the short- and long-time versions of the KD-GSE relation in Eq. (23) for volume fractions from very dilute values to $\phi = 30\%$, and various salt concentrations as indicated. The collective diffusion coefficient, $d_C^S/d_0 \approx d_C^L/d_0$, and high-frequency limiting viscosity, η_∞/η_0, are obtained from the self-part corrected $\delta\gamma$ scheme. The static viscosity, $\eta = \eta_\infty + \Delta\eta$, is calculated using MCT for $\Delta\eta$. Values for $S(q\to 0)$ are obtained from the MPB-RMSA method. Input parameters $L_B = 0.711$ nm, $\sigma = 7.40$ nm, and $|Z| = 10$ are kept constant.

$|Z| = 10$. These parameters are typical of aqueous solutions of small globular proteins such as BSA, Lysozyme[20] and Apoferritin[73]. The charge number Z is kept constant here for simplicity. Theoretical results are plotted as a function of ϕ instead of c_p. In lowering the salt content in Figure 6 stepwise by factors of 0.1, starting from a maximal value of $n_s = 100$ mM, we find that the maximal (positive) deviation from one of the lhs function in Eq. (23) increases roughly logarithmically. For low salt content, $n_s \lesssim 1$ mM, the physical origin of the maxima in Figure 6 is understood from comparing the theoretical results for d_C and η in Figs. 3 and 4, respectively: The maximal violation of the KD-GSE relations occurs roughly at a volume fraction where $d_C(\phi)$ attains its maximum, i.e. for ϕ determined approximately from $k_c^2(\phi) = k_s^2$. Recalling that $k_c^2 \propto \phi$ and $k_s^2 \propto n_s$, this explains why the ϕ-location of the maxima in Figure 6 shows a power-law dependence on n_s for $n_s \lesssim 1$ mM. For larger n_s, a crossover to hard-sphere-like behavior occurs.

6 Conclusions

We have investigated static and dynamic properties of aqueous BSA solutions in an integrated conceptual framework, combining SLS/DLS, SAXS, and rheometric measurements with analytical colloid theory. Solutions with physiological concentrations of added NaCl have been studied, as well as low-salt solutions showing distinct features in the concentration-dependence of the collective diffusion coefficient and the (reduced) viscosity. In our analytical theoretical approach, we

have used a simple spheroid-Yukawa model of BSA with isotropic, repulsive pair interactions to calculate the static scattered intensity using the efficient MPB-RMSA method in combination with the orientational-translational decoupling approximation. The form factor fit has been kept intentionally simple, without expecting extreme accuracy. The resulting $S(q)$ have been used without any further fitting, in calculating d_C, η_∞, and η on basis of our well-tested theoretical methods.

The measured static and dynamic properties of BSA are captured reasonably well in our simplifying SY model, with at least semi-quantitative accuracy, for mass concentrations up to $c_p \approx 100$ mg/ml. In the range 2 mg/ml $\lesssim c_p \lesssim 50$ mg/ml, reliable values for the effective protein charge number, and the residual electrolyte concentration, have been obtained from the fits to the SAXS intensities. The SAXS fits are considerably obstructed for $c_p \lesssim 2$ mg/ml by the presence of scattering impurities, and by the breakdown of the decoupling approximation for $c_p \gtrsim 50$ mg/ml.

A well-developed maximum in the concentration dependence of the collective diffusion coefficient of BSA was found at low salinity. This behavior is seen also in charge-stabilized colloidal suspensions. It is caused by the competition between electrostatic repulsion and hydrodynamic slowing down in crowded systems. Moreover, a non-monotonic concentration dependence of the reduced viscosity of low-salinity BSA solutions was predicted theoretically, and to some extent also seen experimentally. We have explained the local maximum in $\eta_{red}(c_p)$ as a basically non-hydrodynamic effect caused by electric repulsion. A non-monotonic concentration-dependence of η_{red}, with a pronounced peak at low concentration, is observed also in polyelectrolyte solutions. Thus, the low-c_p peak in η_{red} is a generic feature of charge-stabilized dispersions at low salinity.

An essentially concentration-independent underestimation of the experimental d_C and η_{red} by about 25% and 50%, respectively, is made in the theoretical predictions. Possible reasons for this are impurity effects, and an underestimation of the corresponding single-particle coefficients d_0 and $[\eta]$ through our disregarding of the complex protein shape and hydration shell morphology.

We have analyzed the accuracy of a GSE relation by Kholodenko and Douglas[28], which connects the collective diffusion coefficient to the shear viscosity and to the isothermal osmotic compressibility. Despite its appealing simplicity, the KD-GSE relation fails to capture the essential richness of macromolecular collective diffusion. It applies to decent accuracy to electrostatically screened solutions at high salinity, for volume fractions up to about 0.3. However, it is violated for more crowded high-salt solutions, basically for all non-zero volume fractions under low-salt conditions.

The spheroid-Yukawa model for $I(q)$, and the related effective sphere-Yukawa model for the dynamic properties, were used as a minimal model, without including additional protein-specific features such as the complex, non-spherical protein shape, and the non-isotropic distribution of hydrophobic surface patches and surface charges. The overall applicability of this simplified model to describe in particular collective diffusion does not imply that protein-specific properties are of no dynamic relevance. Indeed, the anisotropic protein-protein interaction caused by the non-spherical protein shape and surface patchiness has the tendency to significantly slow the (long-time) translational and rotational self-diffusion in crowded protein solutions, due to the, in comparison to isotropic colloidal spheres, strong direct and hydrodynamic translational-rotational coupling of neighboring particles. The strong effect of the translational-rotational coupling on self-diffusion has been experimentally shown recently for dispersions of charged gibbsite platelets, also in comparison to predictions by the effective sphere model[101]. The gibbsite platelets have an average thickness to diameter aspect ratio of 1 : 11. For the less non-spherical BSA proteins, the translational-rotational coupling effect on the self-diffusion coefficients , and on the viscosity, should therefore be substantially less pronounced. As discussed in Ref.[101] in relation to the gibbsite platelets, the effect of translational-rotational inter-particle coupling is substantially less severe regarding the collective diffusion coefficient, with its practically equal short-time and long-time values. Different from self-diffusion, where the translational/rotational motion of a tagged particle relative to its next-neighbor dynamic cage is probed, collective diffusion describes the cooperative (mean) motion of particles in the direction of a long-wavelength, thermally induced density gradient. The latter type of diffusion is obviously less affected by the translational-rotational coupling. In addition, we note here that attractive inter-particle force contributions such as the van der Waals attraction tend to slow self-diffusion, sedimentation and collective diffusion, and to enlarge the viscosity.

We have commented here only on the general trends expected for non-isotropic and attractive interactions, which have been left out in the present HSY model. For a more detailed analysis, a more refined future modeling of BSA solutions is required. Possible extensions of the present work, which allow to maintain analytical simplicity to some extent, are the inclusion of short-range attractive interactions for suspensions of larger salt content using, e.g. a two-Yukawa pair potential[102,103], and the inclusion of a mean surface patchiness[20]. For the static viscosity of more strongly concentrated protein solutions than considered in the present work, the shear stress relaxation contribution, $\Delta\eta$, can become large in comparison to η_∞. In calculating $\Delta\eta$, one needs then to account for HI contributions which tend to further enlarge its value. Such an inclusion of HI effects into $\Delta\eta$ can be ac-

complished on basis of an extended MCT scheme discussed in Refs.[77,78]. These extensions will be the subject of a future study.

Acknowledgments

M. Heinen is supported by the International Helmholtz Research School of Biophysics and Soft Matter (IHRS BioSoft). F. Zanini acknowledges a fellowship of the Institut Laue Langevin, Grenoble, France. This work was under appropriation of funds from the Slovak grant agency VEGA 0038 for M. Antalík, and VEGA 0155 and CEX Nanofluid for D. Fedunová. F. Zhang and F. Schreiber acknowledge support from the Deutsche Forschungsgemeinschaft. G. Nägele acknowledges support from the Deutsche Forschungsgemeinschaft (SFB-TR6, project B2), and thanks Ch. Gögelein (MPI for Dynamics and Self-Organisation, Göttingen) for helpful discussions.

References

1 P. Ball, *Chem. Rev.*, 2008, **108**, 74–108.
2 R. J. Ellis, *Curr. Opin. Struct. Biol.*, 2001, **11**, 500.
3 S. B. Zimmerman and A. P. Minton, *Annu. Rev. Biophys. Biomolec. Struct.*, 1993, **22**, 27–65.
4 T. Ando and J. Skolnick, *Proc. Natl. Acad. Sci. U. S. A.*, 2010, **107**, 18457–18462.
5 E. J. W. Verwey and J. T. G. Overbeek, *Theory of the Stability of Lyophobic Colloids*, Elsevier, New York, 1948.
6 M. Heinen, P. Holmqvist, A. J. Banchio and G. Nägele, *J. Chem. Phys.*, 2011, **134**, 044532.
7 M. Heinen, P. Holmqvist, A. J. Banchio and G. Nägele, *J. Chem. Phys.*, 2011, **134**, 129901.
8 M. Heinen, A. J. Banchio and G. Nägele, *J. Chem. Phys.*, 2011, **135**, 154504.
9 G. D. J. Phillies, G. B. Benedek and N. A. Mazer, *J. Chem. Phys.*, 1976, **65**, 1883–1892.
10 D. G. Neal, D. Purich and D. S. Cannell, *J. Chem. Phys.*, 1984, **80**, 3469–3477.
11 A. K. Gaigalas, J. B. Hubbard, M. Mccurley and S. Woo, *J. Phys. Chem.*, 1992, **96**, 2355–2359.
12 M. Placidi and S. Cannistraro, *Europhys. Lett.*, 1998, **43**, 476–481.
13 N. Meechai, A. M. Jamieson and J. Blackwell, *J. Colloid Interface Sci.*, 1999, **218**, 167 – 175.
14 W. Bowen and A. Mongruel, *Colloids and Surfaces A: Physicochemical and Engineering Aspects*, 1998, **138**, 161 – 172.
15 Y. X. Yu, A. W. Tian and G. H. Gao, *Phys. Chem. Chem. Phys.*, 2005, **7**, 2423–2428.
16 J. Happel and H. Brenner, *Low-Reynolds-Number Hydrodynamics*, Kluwer, Dordrecht, 1973.
17 F. Roosen-Runge, M. Hennig, F. Zhang, R. M. J. Jacobs, M. Sztucki, H. Schober, T. Seydel and F. Schreiber, *PNAS*, 2011, **108**, 11815–11820.
18 F. Roosen-Runge, M. Hennig, T. Seydel, F. Zhang, M. W. A. Skoda, S. Zorn, R. M. J. Jacobs, M. Maccarini, P. Fouquet and F. Schreiber, *BBA-Proteins Proteom*, 2010, **1804**, 68 – 75.
19 M. L. Broide, T. M. Tominc and M. D. Saxowsky, *Phys. Rev. E*, 1996, **53**, 6325 – 6335.
20 C. Gögelein, G. Nägele, R. Tuinier, T. Gibaud, A. Stradner and P. Schurtenberger, *J. Chem. Phys.*, 2008, **129**, 085102.
21 F. Zhang, M. W. A. Skoda, R. M. J. Jacobs, S. Zorn, R. A. Martin, C. M. Martin, G. F. Clark, S. Weggler, A. Hildebrandt, O. Kohlbacher and F. Schreiber, *Phys. Rev. Lett.*, 2008, **101**, 148101.
22 F. Zhang, S. Weggler, M. J. Ziller, L. Ianeselli, B. S. Heck, A. Hildebrandt, O. Kohlbacher, M. W. A. Skoda, R. M. J. Jacobs and F. Schreiber, *Proteins*, 2010, **78**, 3450–3457.
23 F. Zhang, R. Roth, M. Wolf, F. Roosen-Runge, M. W. A. Skoda, R. M. J. Jacobs, M. Sztucki and F. Schreiber, *submitted*, 2011.
24 A. J. Banchio, G. Nägele and J. Bergenholtz, *J. Chem. Phys.*, 1999, **111**, 8721–8740.
25 J. Bergenholtz, F. M. Horn, W. Richtering, N. Willenbacher and N. J. Wagner, *Phys. Rev. E*, 1998, **58**, R4088–R4091.
26 A. J. Banchio and G. Nägele, *J. Chem. Phys.*, 2008, **128**, 104903.
27 G. C. Abade, B. Cichocki, M. L. Ekiel-Jezewska, G. Nägele and E. Wajnryb, *J. Phys.-Condens. Matter*, 2010, **22**, 322101.
28 A. L. Kholodenko and J. F. Douglas, *Phys. Rev. E*, 1995, **51**, 1081–1090.
29 A. K. Gaigalas, V. Reipa, J. B. Hubbard, J. Edwards and J. Douglas, *Chem. Eng. Sci.*, 1995, **50**, 1107–1114.
30 D. E. Cohen, G. M. Thurston, R. A. Chamberlin, G. B. Benedek and M. C. Carey, *Biochemistry*, 1998, **37**, 14798–14814.
31 P. Boogerd, B. Scarlett and R. Brouwer, *Irrig. Drain.*, 2001, **50**, 109–128.
32 F. Nettesheim, M. W. Liberatore, T. K. Hodgdon, N. J. Wagner, E. W. Kaler and M. Vethamuthu, *Langmuir*, 2008, **24**, 7718–7726.
33 T. Peters, *Adv.Protein Chem.*, 1985, **37**, 161–245.
34 U. Böhme and U. Scheler, *Chem. Phys. Lett.*, 2007, **435**, 342–345.
35 J. Lee and S. Timasheff, *Biochemistry*, 1974, **13**, 257 – 265.
36 A. K. Hunter and G. Carta, *Journal of Chromatography A*, 2001, **937**, 13 – 19.
37 G. Nägele, *Phys. Rep.*, 1996, **272**, 216–372.
38 E. Wajnryb, P. Szymczak and B. Cichocki, *Physica A*, 2004, **335**, 339–358.
39 M. Bano, I. Strharsky and I. Hrmo, *Rev. Sci. Instrum.*, 2003, **74**, 4788–4793.
40 S. Yadav, S. J. Shire and D. S. Kalonia, *Pharm. Res.*, 2011, **28**, 1973 – 1983.
41 K. Monkos, *Biochim. Biophys. Acta*, 2004, **1700**, 27 – 34.
42 D. C. Carter and J. X. Ho, *Adv. Protein Chem.*, 1994, **45**, 153–203.
43 M. L. Ferrer, R. Duchowicz, B. Carrasco, J. Garcia de la Torre and A. U. Acuna, *Biophys. J.*, 2001, **80**, 2422–2430.
44 C. Leggio, L. Galantini and N. V. Pavel, *Phys. Chem. Chem. Phys.*, 2008, **10**, 6741–6750.
45 J. Garcia de la Torre, A. Ortega, D. Amoros, R. Rodriguez Schmidt and J. G. Hernandez Cifre, *Macromol. Biosci.*, 2010, **10**, 721–730.
46 F. Zhang, M. W. A. Skoda, R. M. J. Jacobs, R. A. Martin, C. M. Martin and F. Schreiber, *J. Phys. Chem. B*, 2007, **111**, 251–259.
47 J. S. Pedersen, *Adv. Colloid Interface Sci.*, 1997, **70**, 171–210.
48 D. I. Svergun, S. Richard, M. H. J. Koch, Z. Sayers, S. Kuprin and G. Zaccai, *PNAS*, 1998, **95**, 2267–2272.
49 F. Zhang, F. Roosen-Runge, M. W. A. Skoda, R. M. J. Jacobs, M. Wolf, P. Callow, H. Frielinghaus, V. Pipich, S. Prévost and F. Schreiber, *submitted*, 2011.
50 A. Isihara, *J. Chem. Phys.*, 1950, **18**, 1446–1449.
51 B. R. Jennings and K. Parslow, *Proc. R. Soc. London Ser. A-Math. Phys. Eng. Sci.*, 1988, **419**, 137–149.
52 F. Perrin, *J. Phys. Radium*, 1936, **7**, 1–11.
53 G. B. Jeffery, *Proc. R. soc. Lond. Ser. A-Contain. Pap. Math. Phys. Character*, 1922, **102**, 161–179.
54 F. M. van der Kooij, E. S. Boek and A. P. Philipse, *J. Colloid Interface Sci.*, 2001, **235**, 344–349.

55 M. Kotlarchyk and S.-H. Chen, *J. Chem. Phys.*, 1983, **79**, 2461–2469.
56 W. B. Russel and D. W. Benzing, *J. Colloid Interface Sci.*, 1981, **83**, 163–177.
57 A. R. Denton, *Phys. Rev. E*, 2000, **62**, 3855–3864.
58 J.-P. Hansen and J. B. Hayter, *Mol. Phys.*, 1982, **46**, 651–656.
59 B. J. Yoon, *J. Colloid Interface Sci.*, 1991, **142**, 575–581.
60 E. Eggen and R. van Roij, *Phys. Rev. E*, 2009, **80**, 041402.
61 N. Boon and R. van Roij, *J. Chem. Phys.*, 2011, **134**, 054706.
62 C. Alvarez and G. Tellez, *J. Chem. Phys.*, 2010, **133**, 144908.
63 R. Ramirez and R. Kjellander, *J. Chem. Phys.*, 2003, **119**, 11380–11395.
64 N. Hoffmann, C. N. Likos and J.-P. Hansen, *Mol. Phys.*, 2004, **102**, 857–867.
65 J.-P. Hansen and I. R. McDonald, *Theory of Simple Liquids*, Academic Press, London, 2nd edn, 1986.
66 M. Heinen, P. Holmqvist, A. J. Banchio and G. Nägele, *J. Appl. Crystallogr.*, 2010, **43**, 970–980.
67 C. W. J. Beenakker and P. Mazur, *Physica A*, 1983, **120**, 388–410.
68 C. W. J. Beenakker, *Physica A*, 1984, **128**, 48–81.
69 U. Genz and R. Klein, *Physica A*, 1991, **171**, 26–42.
70 R. B. Jones and R. Schmitz, *Physica A*, 1988, **149**, 373–394.
71 D. J. Jeffrey and Y. Onishi, *J. Fluid Mech.*, 1984, **139**, 261–290.
72 A. J. Banchio, J. Gapinski, A. Patkowski, W. Häussler, A. Fluerasu, S. Sacanna, P. Holmqvist, G. Meier, M. P. Lettinga and G. Nägele, *Phys. Rev. Lett.*, 2006, **96**, 138303.
73 J. Gapinski, A. Wilk, A. Patkowski, W. Häussler, A. J. Banchio, R. Pecora and G. Nägele, *J. Chem. Phys.*, 2005, **123**, 054708.
74 J. Bergenholtz, N. Willenbacher, N. J. Wagner, B. Morrison, D. van den Ende and J. Mellema, *J. Colloid Interface Sci.*, 1998, **202**, 430–440.
75 G. K. Batchelor and J. T. Green, *J. Fluid Mech.*, 1972, **56**, 401–427.
76 W. B. Russel, *J. Chem. Soc., Faraday Trans.*, 1984, **80**, 31–41.
77 G. Nägele and J. Bergenholtz, *J. Chem. Phys.*, 1998, **108**, 9893–9904.
78 A. J. Banchio, J. Bergenholtz and G. Nägele, *Phys. Rev. Lett.*, 1999, **82**, 1792–1795.
79 C. M. Roth, B. L. Neal and A. M. Lenhoff, *Biophys. J.*, 1996, **70**, 977–987.
80 B. Cichocki, M. L. Ekiel-Jezewska, P. Szymczak and E. Wajnryb, *J. Chem. Phys.*, 2002, **117**, 1231–1241.
81 C. Tanford and J. G. Buzzell, *J. Phys. Chem.*, 1956, **60**, 225–231.
82 D. W. Kupke, M. G. Hodgins and J. W. Beams, *Proc. Natl. Acad. Sci. U. S. A.*, 1972, **69**, 2258.
83 R. Curvale, M. Masuelli and A. P. Padilla, *Int. J. Biol. Macromol.*, 2008, **42**, 133–137.
84 S. Förster and M. Schmidt, *Physical Properties of Polymers*, Springer, Berlin, 1995, vol. 120, pp. 51–133.
85 M. Antonietti, A. Briel and S. Förster, *J. Chem. Phys.*, 1996, **105**, 7795–7807.
86 H. Eisenberg, *Biophys. Chem.*, 1977, **7**, 3–13.
87 T. Okubo, *J. Chem. Phys.*, 1987, **87**, 6733–6739.
88 Y. Dziechciarek, J. J. G. van Soest and A. P. Philipse, *J. Colloid Interface Sci.*, 2002, **246**, 48–59.
89 Y. Rabin, *Phys. Rev. A*, 1987, **35**, 3579–3581.
90 S. A. Rice and J. G. Kirkwood, *J. Chem. Phys.*, 1959, **31**, 901–908.
91 K. Nishida, K. Kiriyama, T. Kanaya, K. Kaji and T. Okubo, *J. Polym. Sci. Pt. B-Polym. Phys.*, 2004, **42**, 1068–1074.
92 K. Miyazaki, B. Bagchi and A. Yethiraj, *J. Chem. Phys.*, 2004, **121**, 8120–8127.
93 P. Retailleau, M. Riès-Kautt, A. Ducruix, L. Belloni, S. J. Candau and J. P. Munch, *Europhys. Lett.*, 1999, **46**, 154–159.
94 H. Ohshima, *Langmuir*, 2007, **23**, 12061–12066.
95 J. D. Sherwood, *J. Phys. Chem. B*, 2007, **111**, 3370–3378.
96 M. G. McPhie and G. Nägele, *J. Chem. Phys.*, 2007, **127**, 034906.
97 A. J. Banchio, M. G. McPhie and G. Nägele, *J. Phys.-Condes. Matter*, 2008, **20**, 404213.
98 S. U. Egelhaaf, V. Lobaskin, H. H. Bauer, H. P. Merkle and P. Schurtenberger, *Eur. Phys. J. E*, 2004, **13**, 153 – 164.
99 B. Cichocki, M. L. Ekiel-Jezewska and E. Wajnryb, *J. Chem. Phys.*, 2003, **119**, 606–619.
100 B. Cichocki and B. U. Felderhof, *J. Chem. Phys.*, 1994, **101**, 7850–7855.
101 D. Kleshchanok, M. Heinen, G. Nägele and P. Holmqvist, *Soft Matter, DOI:10.1039/C1SM06735D*, 2011.
102 Y. Liu, W.-R. Chen and S.-H. Chen, *J. Chem. Phys.*, 2005, **122**, 044507.
103 J. M. Kim, R. Castaneda-Priego, Y. Liu and N. J. Wagner, *J. Chem. Phys.*, 2011, **134**, 064904.